Next Materials 1 (2023) 100010

Contents lists available at ScienceDirect

Next Materials

journal homepage: www.sciencedirect.com/journal/next-materials

Review article

One-dimensional metal-organic frameworks: Synthesis, structure and application in electrocatalysis

Xuelei Pan[a,b], Qiuyi Zhu[a], Kesong Yu[a], Mengyu Yan[a], Wen Luo[c,a], Shik Chi Edman Tsang[b,*], Liqiang Mai[a,*]

[a] State Key Laboratory of Advanced Technology for Materials Synthesis and Processing, International School of Materials Science and Engineering, Wuhan University of Technology, Wuhan 430070, PR China
[b] Wolfson Catalysis Centre, Department of Chemistry, University of Oxford, OX1 3QR, UK
[c] Department of Physics, School of Science, Wuhan University of Technology, Wuhan 430070, PR China

ARTICLE INFO

Keywords:
Metal-organic frameworks (MOFs)
One-dimensional
Synthesis
Structure
Electrocatalysis

ABSTRACT

Metal-organic frameworks (MOFs) have been regarded as one of the most promising materials for efficient energy conversion technologies, especially heterogeneous catalysis, since they were initially developed. Recently, one-dimensional (1D) MOFs and their derived materials have shown great potential for electrocatalysis owing to the combination of the characteristics of 1D structure and MOFs, such as favorable charge transfer, adjustable metal center, abundant active sites and porous structure. This review focuses first on the synthesis and structure of 1D MOF materials, and briefly summarizes the application in electrocatalysis. Two main methods, i.e., template-assisted and template-free methods, are introduced by typical examples and the obtained different 1D structures are analyzed. Then the application of 1D MOF and its derived materials are comprehensively described and the structural merits of heterogeneous electrocatalysis are emphasized. Although many 1D MOFs have been developed, exploring a simple and high-yield method to prepare high-crystallized 1D MOF materials for electrocatalysis remains a great challenge. We aim to present the state of the 1D MOFs in the field of electrocatalysis and contribute to the rational design and synthesis of 1D MOFs.

1. Introduction

With the rapid development of the industrial economy, upgrading energy structure has become increasingly prominent, thereupon, the exploitation of sustainable and clean energy has become an urgent need [1–3]. In a sustainable energy system, electricity, as one of the fundamental energy forms, can be obtained from tremendous forms of renewable energy, e.g. solar energy [4], wind power [5], hydraulic energy [6], etc. Therefore, developing efficient methods to converse and store electricity is a project of great importance [7,8]. As a typical energy conversion form, electricity can be stored in energetic molecules [9,10], e.g., H_2, which can be used to supply chemical energy [11,12]. Chemical energy conversion based on electricity (such as electrocatalytic technology [13–16]) is a feasible way to relieve the increasing energy issues and provide clean fuels for industrial manufacture [1]. The core of electrochemical catalysis technology is using high-performance electrode materials to achieve efficient energy conversion, and consequently, the development of electrocatalysts has become the current research focus [17–20].

Traditional electrocatalysts are mainly noble metals and their compounds, showing low overpotential and fast reaction kinetics [21–23]. However, rare reserves and the high cost of the noble metal catalyst limit further development. In recent years, research on non-noble metal catalysts has expanded to new material systems with explicit and controllable active sites, such as single-atom catalysts [24–26], metal-organic frameworks (MOFs) [27–29], etc. MOFs are organic-inorganic hybrid materials formed by self-assembling organic ligands and metal ions/clusters, which present a typical porous structure [30,31]. The distinct characteristics of MOFs are a large specific surface area, adjustable pores, and functionalization [32,33]. In 1995, Yaghi et al. synthesized two-dimensional materials through the reaction of cobalt and 1,3,5-benzenetricarboxylic acid (BTC), and proposed the concept of metal-organic frameworks for the first time [34]. Due to MOF's unique coordination connection mode, various metal centers and organic ligands can be paired. Therefore, MOF can exhibit structures of various dimensions and has been widely used in gas adsorption/storage [35,36], biocatalysis [37,38], photocatalysis [39,40], electrocatalysis [29,41] and energy storage, etc.

* Corresponding authors.
E-mail addresses: edman.tsang@chem.ox.ac.uk (S.C.E. Tsang), mlq518@whut.edu.cn (L. Mai).

https://doi.org/10.1016/j.nxmate.2023.100010
Received 5 February 2023; Received in revised form 17 March 2023; Accepted 18 March 2023

In recent years, intensive effort has been paid to developing low-dimensional MOFs [41–44]. Low-dimensional MOF materials have characteristics of large surface area, controllable structure, and pore diversity of MOF materials [45,46], as well as the unique physical/chemical properties of low-dimensional nanomaterials, such as high aspect ratio, rich active sites, and good flexibility [47–49]. These merits of low-dimensional MOF have promoted its applications in various aspects. Taking their application in electrocatalysis as an example, low-dimensional MOF has a large surface area and abundant transition metal (such as cobalt, zinc, iron)/inorganic (especially nitrogen) active sites, adjustable porosity, which can expose more active sites and expand the pores of the material to enhance catalytic activity and stability [41,46]. In addition, a well-organized and tightly fabricated MOF array can improve charge transfer and enhance the electrochemically active surface area [50,51]. Although low-dimensional MOFs favor better catalytic activity, in some cases, MOFs tend to collapse, agglomerate, and inhibit diffusion in catalytic reactions [52]. Different from other low-dimensional MOFs, one-dimensional (1D) MOFs possess similar morphological characteristics to the 1D structure, i.e., the unique geometric and electronic properties, which facilitate the design of the promising electrocatalysts [46,53,54]. Electrocatalysts based on 1D MOF materials, such as pure MOF electrocatalysts [55,56], MOF-supported composite electrocatalysts [57,58] and MOF-derived electrocatalysts [59,60], etc. have been investigated in tremendous heterogeneous electrocatalysis, such as hydrogen evolution reaction (HER), oxygen evolution reaction (OER), oxygen reduction (ORR), carbon dioxide reduction (CO_2RR), etc. Researchers have studied the structure, conductivity, and stability of MOFs to obtain higher catalytic activity. Concerning structure regulation, researchers have synthesized 1D MOFs with various structures through the template-assisted method and the template-free approaches. For instance, the zeolitic imidazolate framework-8 (ZIF-8) is a typical MOF material with a large pore volume, surface area, and high thermal and chemical stability [61]. This material can be prepared based on the reaction of a soluble metal salt (zinc nitrate) with an organic ligand in the solvent [62,63] or using 1D ZnO as a template to form a 1D structure [64–66]. Although 1D structure can be controllably achieved, the conductivity of MOFs is still a remaining issue, which limits the direct utilization of MOFs as electrocatalysts. Up to now, many works still use 1D MOFs as precursors to achieve metal compounds on the conductive carbon substrate, which is commonly used to increase conductivity in HER and ORR. With the development of electrically conductive MOFs [67], the direct use of MOFs as electrocatalysts brings new opportunities for studying the fundamental structure-property relationships of MOF catalysts. With the aim for practical application, the stability of MOFs is another crucial point [68]. The stability of MOFs mainly relies on the coordination strength between the metal site and ligand, which directly influences the structure in acidic/alkaline electrolyte. Another issue is that the valance state is modulated by electrode potential in electrocatalysis, which could result in structural collapse. Hence, robust and highly active 1D MOFs are desirably investigated for electrocatalysis research, which is a challenging but significant subject.

Based on the principle of application of 1D MOF materials in electrocatalysis, this review aims to summarize the structure of 1D MOF prepared by different synthesis methods, and further analyze and discuss the progress and challenges of the application of 1D MOF materials in electrocatalysis. Last, a perspective for the future of 1D MOFs has been proposed. This review is expected to contribute to developing MOF-based electrocatalysts for clean energy conversion.

2. Fundamental principles of 1D MOF in electrocatalysis

The reduced size of 1D nanomaterials contributes to the unique characteristics that differ from bulk nanomaterials. For example, in catalysis, nanocrystals usually expose more active sites involved in adsorbing reactants due to their larger surface area [74,75]. MOFs are considered as a class of electrocatalysts with broad development prospects due to their high specific surface area, porousness, structural controllability, and highly dispersed single-metal sites [76,77]. 1D MOFs possess characteristics of both 1D structures and MOFs, and have been researched for electrocatalysis in recent years (Fig. 1).

Electrocatalysis is a kind of catalysis in that a chemical reaction is driven by electrode voltage on the interface of electrode and electrolyte, whereby reactants couple with electrons to form intermediates or products [3]. Heterogeneous electrocatalysis can be assumed to include two aspects: charge/mass transport and interface reaction [78,79]. Therefore, the electrocatalyst should be able to transfer electrons efficiently and effectively catalyze and activate the reactant [80]. Most 1D MOFs show slow charge transfer due to the lack of continuous electron transfer pathways in organic ligand frameworks, which inhibit the activity of MOFs to some extent and result in works on some MOF-derived catalysts rather than MOF catalysts. Similarly, although the porosity of MOFs enables a large surface area, the mass transfer in a liquid electrolyte cannot be promoted due to the small pores (smaller than 2 nm). Generally, the challenges of designing a high-performance catalyst can be mainly categorized into the following four aspects:

1. Intrinsic catalytic activity: The most critical issue in designing a catalyst is finding a rational method to describe intrinsic catalytic activity [81,82]. With the development of computational methods, fundamental physical properties, such as electronic structure [83,84], binding energy [85], and coordination structure [86] are involved in building descriptors of catalytic activity. However, up to now, descriptors usually have some limitations when applied to new materials systems, which results in difficulty in predicting and describing the intrinsic catalytic activity. The descriptor of intrinsic catalytic activity of MOFs is still an essential issue for designing MOF catalysts.
2. Active sites: Another critical challenge is determining active sites in a complex system [87–89]. Besides the ideal single-crystal system, the practical catalysts can be complex in component, crystal structure, and morphology. For MOF catalysts, the activities are generally recognized as metal sites, although in some cases, the coordination environment strongly influences the activity [90]. Meanwhile, MOF catalysts may undergo reconstruction to a different degree, which causes more indeterminacy in active sites [91–93].
3. Charge/mass transportation: The charge transfer in electrode and mass transport in electrolyte both impact the reaction kinetics [94–96]. Besides noble metal catalysts, transition metal compounds are influenced by the charge transfer in the catalyst. The improvement of charge/mass transport is essential to design a practical catalysis system [97]. Some strategies can be applied in designing 1D MOF electrocatalysts, such as designing $\pi - \pi$ stacking MOFs to realize high electrical conductivity and construct a hierarchical structure to optimize mass transfer [98].
4. Poor stability: To achieve high ion conductivity, the electrolyte in the electrocatalytic system is usually highly concentrated, which means strong corrosion and damage to catalysts [99,100]. Hence, reconstruction, dissolution, and aggregation occur in most catalytic systems, let alone MOF catalysts. On the one hand, this phenomenon contributes to the formation of new active components that increase efficiency [101]. On the other hand, the drastic structural degradation would result in poor stability and lead to the failure of the MOF catalysts [102].

The structural porosity, crystal structure, and electronic band structure of MOFs are all crucial factors that regulate their electrocatalytic performance. Bulk MOF materials are rarely used in HER, OER, and ORR, and their electrocatalytic performance is normally limited by slow mass transfer and charge transfer processes [103]. Because the size of micropores is commonly too small, the mass transfer rate cannot be adapted to the high turnover frequency (TOF) of the

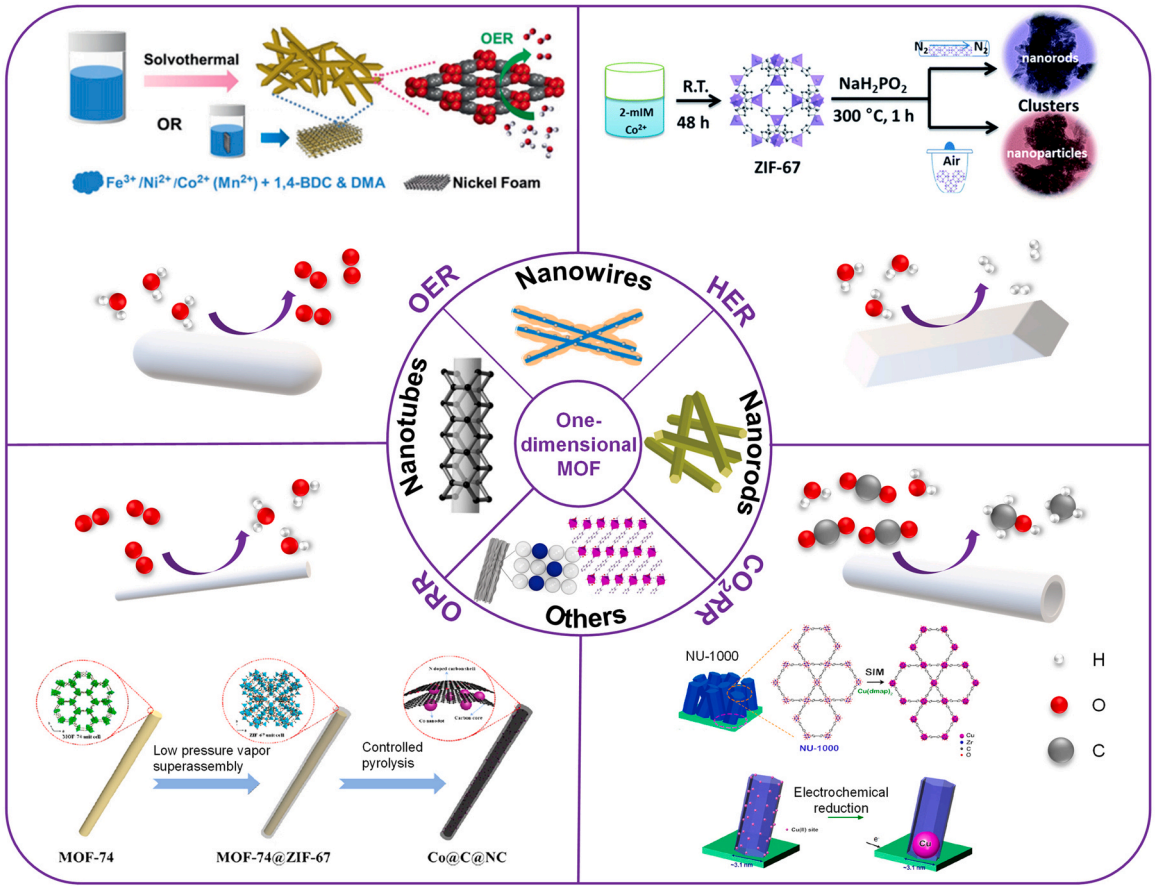

Fig. 1. Summaries of 1D MOFs and their applications in electrocatalysis. Upper left: representative example of 1D MOF-based materials used for OER [55]. Upper right: representative example of 1D MOF-based materials used for HER [69]. Lower left: representative example of 1D MOF-based materials used for ORR [59]. Lower right: representative example of 1D MOF-based materials for CO_2RR [57]. Center: Representative examples of the structure of 1D MOFs, nanorods [70], nanowires [71], nanotubes [72], others [73].

reaction process, which ultimately brings up the mass-transfer-controlled electrocatalytic process. Moreover, most bulk MOFs are insulators or semiconductors with significant band gaps, and their conductivity is too poor to meet the requirement of electrochemical reactions [104].

Compared with the poor conductivity of bulk MOF materials, the 1D MOF structure has a well-defined 1D channel for electron transfer [44,105]. In addition, since the apparent activity of the electrocatalysts depends on the intrinsic activity of individual active sites and the density of active sites, 1D MOF possesses abundant active sites and can be used for the adsorption and transformation of reactants, so theoretically high apparent activity can be achieved. At the same time, the unique framework structure of the aggregated 1D MOF material provides a continuous channel for the infiltration of electrolytes, which favors the interfacial charge transfer in the electrocatalytic reaction. More importantly, the porosity of versatile MOF can be tuned concerning specific catalytic processes (reactant adsorption/desorption) to ensure the high stability of the 1D structure. In this regard, 1D MOF holds great promise for designing high-performance electrocatalysts in terms of activity, structural merits, and stability.

3. Synthesis and structure of 1D MOFs

3.1. Synthesis of 1D MOFs

One characteristic of the 1D structure is the orientation along a specific direction, which enables directional electron transport [106]. The characteristics of MOFs, e.g., high porosity, large specific surface area, etc. are critical to enhancing the electrochemically active surface area. MOFs with 1D structure, e.g., nanorods, nanotubes, and nanowires, have unique physicochemical properties and electrocatalytic properties due to the combination of the characteristics of the 1D structure and the performance of MOF materials and have attracted researchers' attention. Currently, two main methods are used to achieve 1D MOF (Fig. 2): template-assisted and template-free methods. Below, these two methods will be briefly introduced with some typical examples.

3.1.1. Template-assisted method

The template-assisted method is usually realized by depositing MOF materials into the channel or onto the surface of a controllable 1D template structure through physical or chemical methods and then removing/keeping the template to persist the shape of the template. The template-assisted method is a commonly used approach to prepare 1D MOF, effectively controlling the morphology and composition and realizing the large-scale preparation. Specifically, the template-assisted method used to prepare 1D MOF can be classified into the hard template method and the sacrificial template method.

A typical process of the hard-template method to synthesize 1D MOF structure mainly involves the nucleation and crystal growth of MOFs on the external/internal surface of the 1D template. Among them, a polycarbonate track-etched (PCTE) membrane is a typical hard template with 1D channels to confine the growth of 1D MOFs (Fig. 3a). Arbulu et al. constructed 1D ZIF-8 nanostructures and superstructures by changing the size of the pores of the PCTE membrane template and the type or concentration of reactants, and obtained 1D ZIF-8 with nanorods, nanotubes, and nanowires structures [107]. In detail, they used PCTE film as a template, $Zn(NO_3)_2{\cdot}6\,H_2O$, and 2-methylimidazole as reactants for

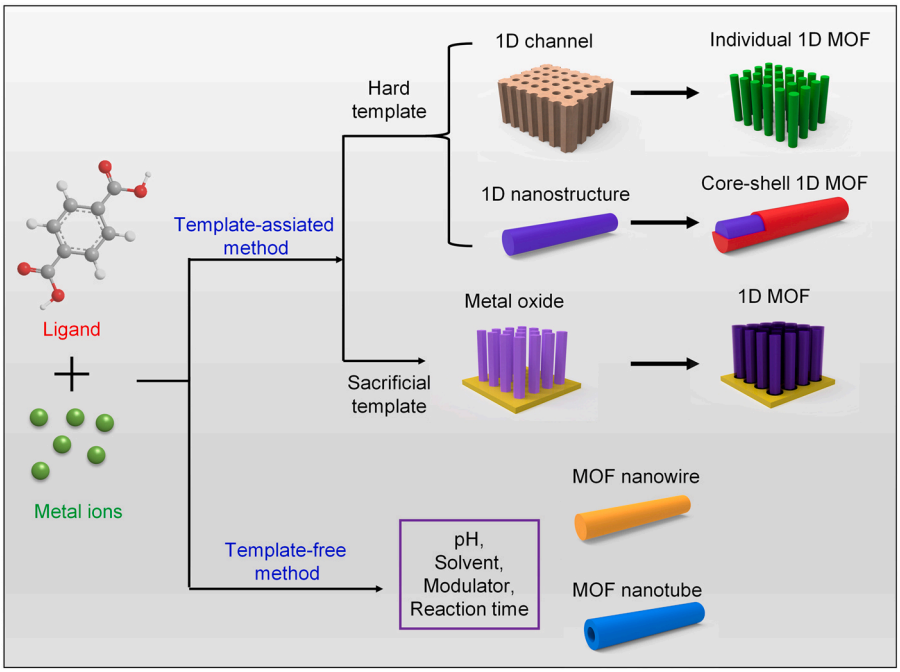

Fig. 2. Schematic illustration of two typical preparation strategies for MOFs with 1D structure.

interfacial synthesis (Fig. 3b). After the template was dissolved, ZIF-8 nanorods were obtained in 100 nm membrane pores (Fig. 3c). They also found that when $Zn(Ac)_2$ was used instead of $Zn(NO_3)_2{\cdot}6\,H_2O$, ZIF-8 nanotubes were obtained. Meanwhile, when a PCTE film with a smaller pore size of 30 nm was used as a template for the reaction, single crystal ZIF-8 nanowires were obtained. In addition to the 1D channel-based template, 1D inorganic nanostructures are feasible templates. For example, hydroxyapatite (HAP) nanowires (loaded with Fe_3O_4 nanoparticles, denoted as mag-HAP nanowires) can be used as the template to fabricated 1D MIL-100 (Fe-MOF) (Fig. 3d,e) [71]. This fabrication process was realized based on the rich active sites of HAP nanowires, and the Fe MOF was assembled layer-by-layer. In another case, silicon nanowires were used as the template to synthesize 1D MOF-199 (HKUST-1) [108]. The Si nanowires were treated by oxygen plasma and anhydrous toluene solution to form -COOH groups ultimately, which contributes to the growth of 1D MOF on Si nanowires.

Based on 1D hard templates, the synthesis of 1D MOF can be easily realized, while the hard template method usually requires specific surface modification on the template to regulate the growth of 1D MOF materials. More importantly, the synthesis process is often cumbersome and complicated, and the 1D structure will likely collapse while removing the template. Different from the hard template, the sacrificial template method based on metal oxide or hydroxide nanostructures does not require functional treatment of the template surface and is also an effective and controllable synthesis method. In the sacrificial template method, the particles used as the template can also be used as reactants to participate in the construction process of the 1D structure, thereby controlling the size and shape of the 1D MOF structure. For example, ZnO can be synthesized as abundant nano-scale morphology (e.g., nanorods, nanobelts, nanotetrapods, nano rings, nanocombs and nanopyramids, etc.), which can be used as a sacrificial template. For instance, Zhan et al. applied 1D ZnO nanorods as a sacrificial template to synthesize ZnO@ZIF-8 nanorods with a chemical bath process in a mixed solvent of N,N-dimethylformamide (DMF) and water [65]. In this process, ZnO is the only source of Zn^{2+} to coordinate with 2-methylimidazole and form a ZIF-8 layer on individual ZnO nanorods (Fig. 3f,g). Another example shows a route to achieve the complete conversion of inorganic hydroxides to 1D MOF. Wang et al. used hydroxide nanostructures as precursors to synthesize a series of ultra-thin MOF nanoribbons (Fig. 3h,i) [109]. Typically, $Co(OH)_2$ and $Ni(OH)_2$ nanoplates were used to react with 1,4-benzenedicarboxylate (BDC) to prepare CoBDC and NiBDC nanoribbons (NRBs), respectively. In this process, the growth of MOF is controlled by releasing metal ions from metal oxide nanostructures. Different from the ZnO-based route, this strategy obtained pure 1D nano MOF without the inorganic core, which can be considered as a simple and efficient approach.

3.1.2. *Template-free method*

Although the template-assisted method has been widely applied, the synthesis process is sophisticated, and template removal is difficult. The direct synthesis of 1D structure earns more attention.

A series of works on developing template-free methods to prepare 1D MOF have been reported, such as the addition of coordination modifiers to control the nucleation and growth to form 1D MOF, which is a simple and effective method. As a typical MOF with a 1D channel, MOF-74 can be easily controlled to form a 1D structure with a series of metal ions as nodes (e.g., Zn^{2+}, Ni^{2+}, Co^{2+}, Fe^{2+}, Cu^{2+}, Mg^{2+}). The growth of MOF-74 can be adjusted by controlling the pH and adding a modulator. The high pH leads to the strong deprotonation of the ligand and results in fast nucleation, which does not favor the growth of nanocrystals as well as the 1D structure. Similarly, adding a specific modulator can facilitate crystal growth and suppress nucleation. Based on these two criteria, the controllable synthesis of 1D MOF-74 has been investigated. Wu et al. found that the morphology of Mg-MOF-74 is related to pH, which means 1D Mg-MOF-74 can be achieved when pH is between 8.63 and 9.55 [110]. Based on the precise control of 1D MOF nanocrystals, they further achieved the core-shell MOF-74 and hollow MOF-74 (Fig. 4a). As shown in Fig. 4b, they also monitored the growth process from a fusiform-shaped crystal to a longer and well-defined 1D MOF-74. Wang et al. adjusted the nucleation rate of MOF during the merge of pre-synthesized active nanoparticles to control the crystal size, and reduce the size of the MOF [111]. 1D MOF was obtained by reducing the surrounding MOF crystal, and the MOF crystal smaller than 50 nm was synthesized.

Besides, changing the reaction solvent can also effectively control the morphology of 1D MOFs. Xu group reported the synthesis of MOF-74 with different metal nodes in different solvents (methanol and DMF) to achieve 1D Co-MOF-74 and Zn-MOF-74 through a simple hydrothermal method [70,112]. Bataille et al. used a "bottom-up" approach to

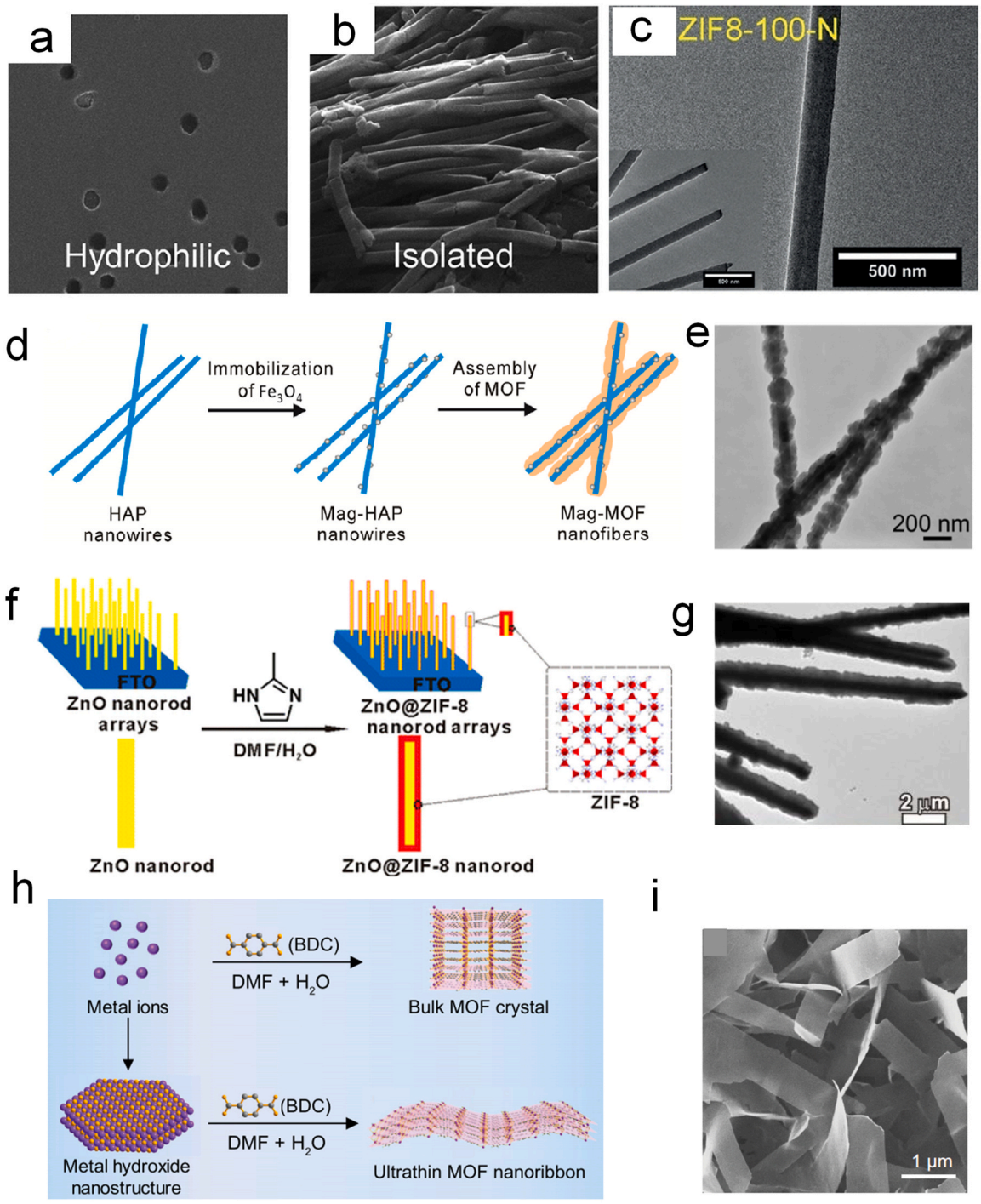

Fig. 3. (a) Scanning electron microscopy (SEM) images of the hydrophilic and membrane surfaces (b) Isolated nanostructures of ZIF8–100-N. The width of (a) and (b) are 2 mm and 4 mm, respectively. (c) Transmission electron microscopy (TEM) images of ZIF8–100-N. (d) Illustration of the fabrication process of mag-MOF nanofibers. (e) TEM images of mag-MOF nanofibers. (f) Schematic illustration of ZnO@ZIF-8 nanorods synthesized via the self-template strategy. (g) Low-magnification TEM image of ZnO@ZIF-8 nanorods. (h) Comparison of the traditional approach to bulk MOF crystal and metal-hydroxide nanostructure precursor approach to ultra-thin MOF nanoribbon. (i) SEM images of the as-prepared CoBDC NRBs.
(a-c) Reproduced from [107]. (d,e) Reproduced from [71]. (f,g) Reproduced from [65]. (h,i) Reproduced from [109].

obtain nanoparticles directly by changing the synthesis conditions of related microcrystals (Fig. 4c,d) [113]. Through the reaction of copper (II) acetate monohydrate, H_2pcp and bpye (pcp = P,P'-diphenyl-diphosphinate, bpye = 1,2-bis(4-pyridyl)ethane) in warm water, they obtained $[Cu_2(pcp)_2bpye]\cdot 2.5\,H_2O]_n$ with long needle crystals structure. This 1D MOF compound was formed by single-walled tubes connected by weak van der Waals interactions. When the above synthesis was carried out in pure ethanol solvent, MOF nanorods were obtained. However, this method is only suitable for bulk crystal structures, and the further separation and achieving individual nanostructures remain to be solved. Considering the fabrication of MOF nanoparticles, electrospinning was also considered as a facile method to achieve 1D nanostructures, although the MOF particles are not continuous in terms of crystal structures [114,115]. This method is widely adopted in the

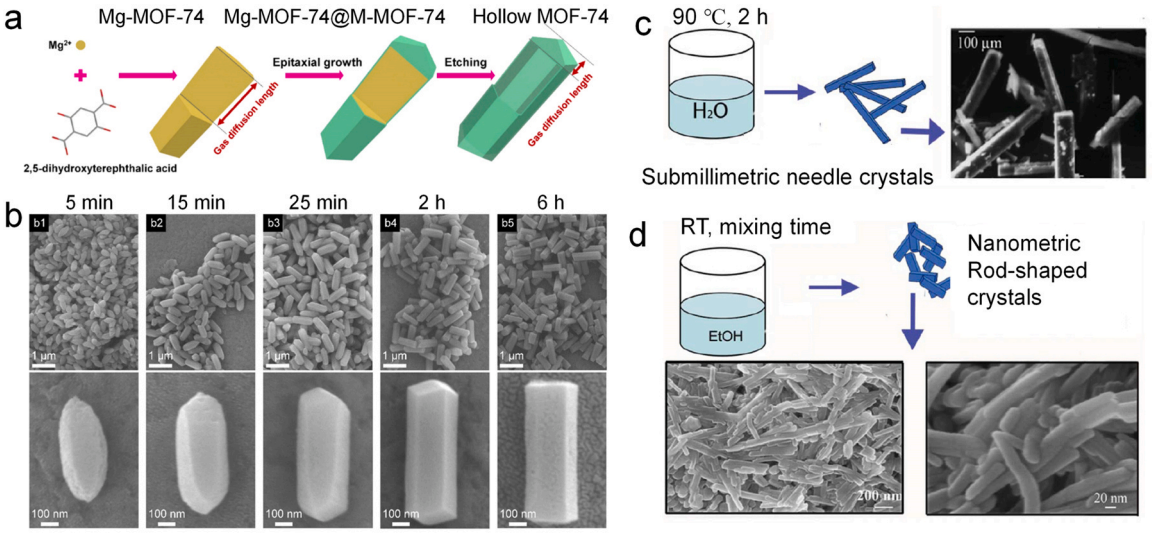

Fig. 4. (a) Synthetic Procedures for Mg-MOF-74, Core – Shell, and Hollow MOF-74. (b) SEM images of Mg-MOF-74 synthesized with an increased reaction time. (c,d) Effect of the solvents on size of the obtained 1D-MOF: (c)synthesis of needle microcrystals from water and (d) synthesis of MOF nanorods from ethanol.
(a,b) Reproduced from [110]. (c,d) Reproduced from [113].

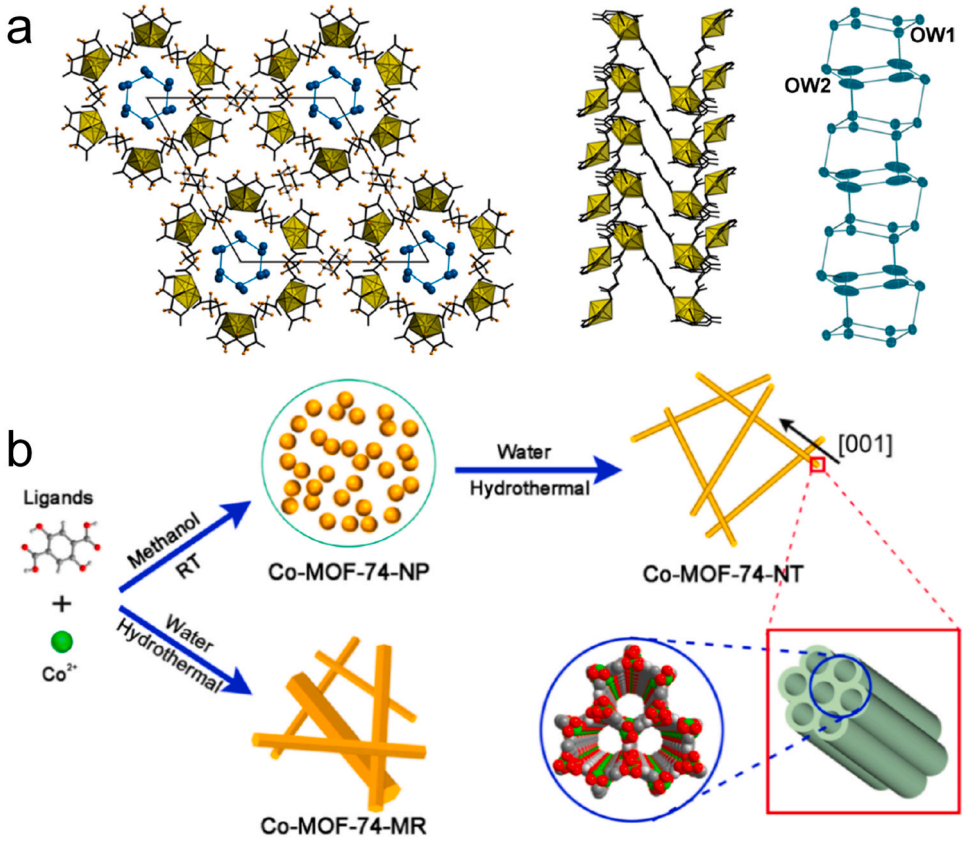

Fig. 5. (a) UMON contains hexagonally packed water molecules within nanotubular structures. (b) Scheme of synthesis of Co-MOF-74-NT (nanotube) and Co-MOF-74-MR (Co-MOF-74 rods in a micrometer scale with a low aspect ratio).
(a) Reproduced from [118]. (b) Reproduced from [112].

fabrication of 1D MOF-derived materials, which will be discussed in the section of the application.

Different from the channel-like MOFs, some layered MOFs can also be synthesized into 1D structures. According to the coordination chemistry, the growth of layered MOFs is not dominated by the strong in-plane metal-ligand bonds but by the out-of-plane weaker π-stacking interactions. This feature causes the tendency to grow to one dimensional or needle shape, whereas the crystal can be disordered along the axis due to the weak interaction. Dincă et al. reported a series of π-conjugated conducting MOFs [116,117]. The designed ligand (2,3,7,8,12,13-hexahydroxybtetraazanaphthotetraphene (HHTT)) weakens the in-plane coordinate bond and enhances out-of-plane π-stacking interaction, contributing to the anisotropic crystal growth. This work systematically demonstrates adjusting crystal orientation by

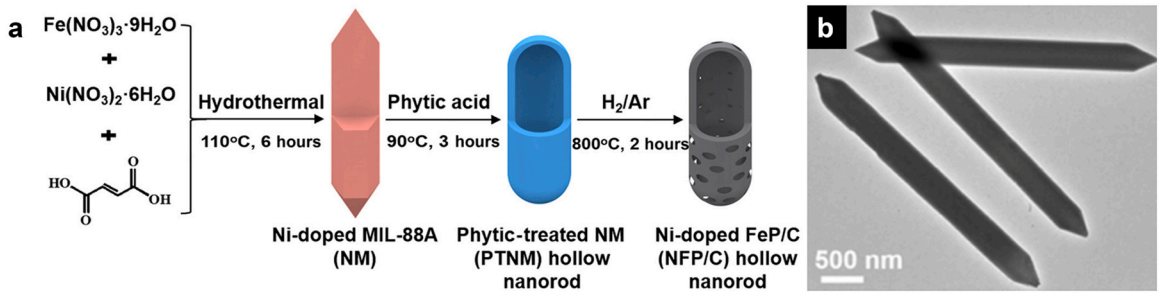

Fig. 6. (a)Schematic illustration of the formation of Ni-doped FeP/C hollow nanorods. (b)TEM images of MIL-88A. Reproduced from [120].

precisely modifying the coordination environment.

To sum up, compared to template-assisted methods, the template-free synthesis process is more straightforward concerning template selection, surface modification, and template removal. Meanwhile, compared with the abundant available nanocrystalline structure in the template-assisted method, the direct synthesis (template-free method) of 1D MOF is limited due to the difficulty in precise and adjustable control of crystal orientation. The large-scale synthesis of 1D MOFs with controlled size and structure is still challenging and needs more investigation in coordination chemistry.

3.2. Structure of 1D MOFs

Due to the unique morphology and structure of 1D MOFs, they present unique physical and chemical properties and are widely used in gas adsorption, heterogeneous (electro)catalysis, electrochemical supercapacitors, metal-ion batteries, and other fields. According to the apparent morphological structure of 1D MOF materials, they can be roughly divided into nanotubes, nanorods, and nanowires. Herein, the characteristics of these 1D MOF structures are introduced.

3.2.1. Nanotubes

Nanotubes are hollow cylindrical structures with a 1–100 nm diameter range. Nanotube materials have unique characteristics in molecule transport and storage and can be applied in sensors, ion separation, catalysis, and drug delivery. Due to the difficulty of self-assembly, only several successful methods have been reported to prepare the nanotube structure of MOFs. For example, Unruh et al. used supramolecular methods to synthesize a new metal-organic nanotube, $(C_4H_{12}N_2)_{0.5}[(UO_2)(Hida)(H_2ida)]\cdot 2\,H_2O$ (UMON) (Fig. 5a) [118]. Under ambient conditions, they synthesized UMON by mixing uranium nitrate, piperazine and iminodiacetic acid in a water/methanol solution. The X-ray diffraction characterization result at liquid-N_2 temperature shows a stacked macrocyclic array and the unique structural arrangement of water molecules inside the nanotube. The thermogravimetric analysis results show that the water molecules inside the nanotubes are completely removed from the tunnels at 37 °C, while the MOF structure can be maintained until 250 °C. Combined with the XRD data of the UMON single crystal when heated to 80 °C, the special selectivity of water absorption inside the nanotube is confirmed. Zou et al. reported a new strategy for amorphous MOF to regulate recrystallization (Fig. 5b) [112]. By regulating the dissolution and recrystallization process of amorphous MOF in a solvent, the diameter and length of MOF nanocrystals were controlled, and ultra-long single-crystal MOF nanotubes were achieved. The obtained MOF nanotubes can be used to separate dye macromolecules in aqueous solutions, and can also be used as precursors to prepare three-dimensional dendritic nanostructures.

3.2.2. Nanorods

Generally speaking, a nanorod is typically defined as a rod-like nanostructure with a length-to-diameter ratio of around 3–5. Nanorods have been extensively used in many areas, such as chemical carriers, composites, and adsorbents [119]. For instance, Lu et al. reported the hydrothermal synthesis of Ni-incorporated MIL-88A hexagonal nanorods by using fumaric acid as a ligand (Fig. 6) [120]. The ratio of Ni and Fe was adjusted to control the length-diameter ratio. It is demonstrated that the increased Ni-Fe ratio results in a smaller medium-length-diameter ratio. Researchers further treated the as-prepared Ni-incorporated MIL-88A nanorods with the phytic acid solution to etch the core and obtained a hollow nanorod. In order to apply in electrolysis, the obtained hollow nanorod was thermally treated and derived Ni-doped FeP/C material perfectly maintains the hollow nanorod structure. Owing to its abundant active sites of a 1D hollow structure, the Ni-doped FeP/C materials exhibit optimized HER activity. The overpotentials at the current density of 10 mA/cm^2 in acidic, neutral, and alkaline electrolytes are 72, 117, and 95 mV, respectively. Similarly, Pachfule et al. reported the synthesis of MOF-74 nanorod by a mild reaction at room temperature [70]. In this process, the salicylic acid stabilized the surrounding active surface and regulated the oriental growth of MOF into a rod-shaped structure. Subsequently, MOF-74 nanorods were used as the precursor to obtain graphene nanoribbons due to the well-defined nanorod structure.

3.2.3. Nanowires

Nanowires are generally tens to hundreds of micrometers long with a large length-diameter ratio and randomly oriented in a straight or curved form. Due to their unique structure, nanowires show great potential in fabricating porous 3D electrodes for catalysis. Zhu et al. synthesized phosphonate MOF nanowires (TiPNW) through a simple sol-gel chemistry method (Fig. 7a,b) [121]. The obtained TiPNW behaves as a hybrid semiconductor under light, which can be applied in stable water photolysis to produce H_2. It was demonstrated that the organophosphorus ligand could regulate the bandgap of MOF through the electron-donating -OH group, which enhances the photocatalytic activity. This work demonstrated the possibility of adjusting the electronic structure of phosphonate-based MOFs through the rational functionalization of organic ligands and showed new ideas for developing advanced photocatalysts with designed structures and electronic properties. In another case, Zhang et al. have demonstrated the nanowire-directed template synthesis of MOF nanofibers (Fig. 7c,d) [122]. The ultra-thin tellurium nanowires (TeNWs) were used as the template to synthesize oriented ZIF-8 nanocrystals and form uniform ZIF-8 nanofibers. The diameter and crystallinity of ZIF-8 nanofibers can be adjusted by controlling the concentration of TeNWs. After freeze-drying to maintain the 3D scaffold structure, the prepared ZIF-8 nanofibers can be further converted into porous carbon nanofibers by thermal treatment.

3.2.4. Other 1D structures

In addition to the above three typical 1D structures, the complex network, hybrid structures, and nanoarrays structures are easily achieved and are composed of fundamental 1D nanostructures. For example, Huang et al. introduced Cu^{2+} into MIL-53 series MOFs (Al-MIL-53) and achieved a stable MOFs catalyst with a cross-linked

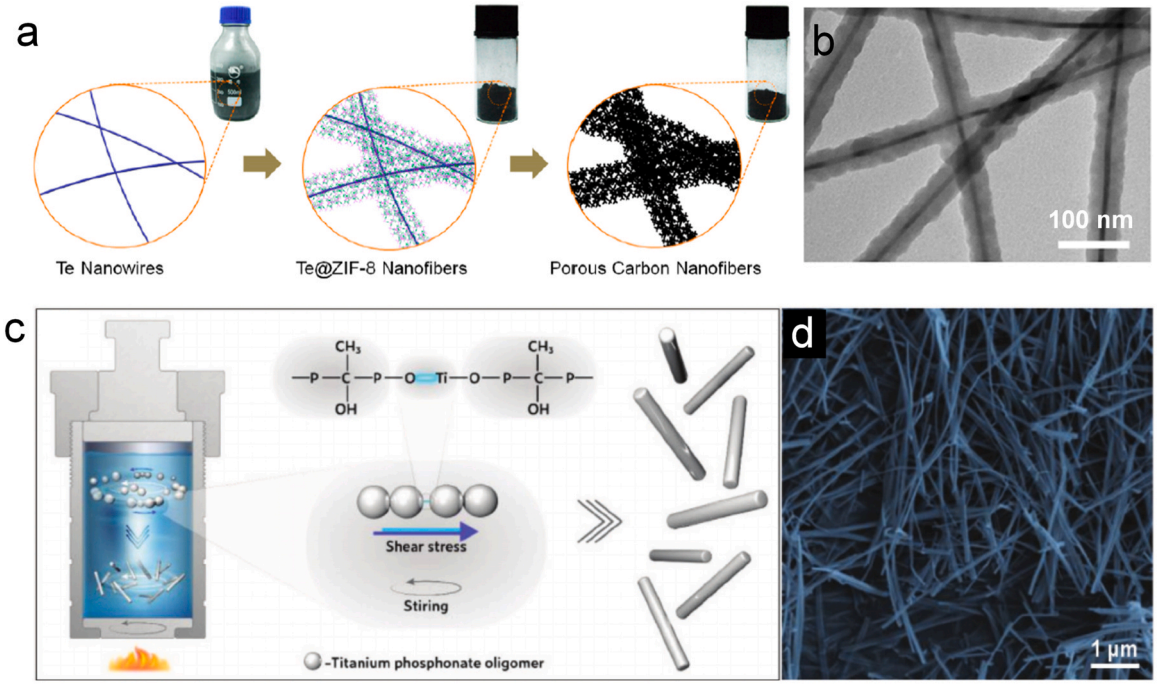

Fig. 7. (a) Illustration of the nanowire-directed templating synthesis of ZIF-8 nanofibers and derived porous doped carbon nanofibers. (b) TEM images of as-prepared Te@ZIF-8 by regulating the amounts of precursors. The average diameter corresponds to 45 nm; the scale bar: is 100 nm. (c) The synthesis scheme of the titanium phosphonate nanowires. (d) SEM images of TiPNW.
(a,b) Reproduced from [121]. (c,d) Reproduced from [122].

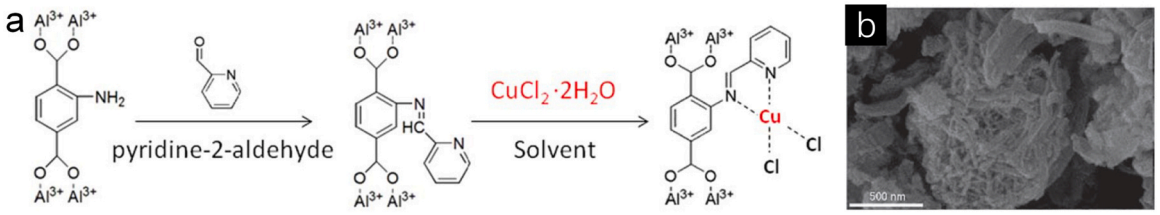

Fig. 8. (a) Post-synthetic modification of Al-MIL-53-P21 with pyridine-2-formaldehyde and Cu(II). (b) SEM image of the carrier NH_2-MIL-53(Al). Reproduced from [123].

nanorods network structure (Fig. 8) [123]. In this work, Al-MIL-53-NH_2 was first obtained through the reaction of Al^{3+} and NH_2-BDC. When preparing Cu-incorporated MOF, the pyridine-2-formaldehyde was introduced to provide an aldehyde group and react with -NH_2 to form an N-containing ligand. With the incorporation of Cu^{2+}, the obtained MOF becomes a nanorod under the coordination of pyridine-2-formaldehyde and Cu^{2+}. This MOF is a new and stable 1D MOF (Cu@Al-MIL-53-P21) with good crystallinity. Moreover, the Cu@Al-MIL-53-P21 nanorod can promote the formation of benzaldehyde with high efficiency and reduce the production of by-products.

4. Applications in electrocatalysis

Among the tremendous electrocatalysts, 1D MOFs have become a potential hotspot in electrocatalysis in recent years due to their high porosity, ultra-high specific surface area, and rich active sites. However, the poor conductivity and low-crystalline of 1D MOF materials make it difficult to meet the performance and stability requirements of electrocatalysis technology, limiting its application [124]. Therefore, compositing or encapsulating other nanomaterials with MOFs, such as metal nanoparticles, quantum dots, etc., or calcined into core-shell or hollow structures or arrays to synthesize 1D MOF-based materials, have been widely investigated to improve the electrocatalytic performance of MOF materials. The performance of different MOFs is summarized in Table 1. Herein, the application of electrocatalysts based on 1D MOF materials in electrochemical water splitting, oxygen reduction, and carbon dioxide reduction is introduced.

4.1. Electrocatalytic water splitting

The electrocatalytic water splitting contains two half-reactions, i.e., hydrogen evolution reaction (HER) and oxygen evolution reaction (OER) [125]. Both meet some critical issues, such as slow reaction kinetics, especially OER goes through multiple proton-coupled electron transfer (PCET) steps and involves the transfer of four electrons [17,126]. For developing efficient electrocatalytic water splitting technologies, high-performance electrocatalysts are introduced to reduce energy barriers and enhance reaction kinetics. At present, the most efficient catalysts for electrochemical water splitting are precious metals and their oxides (Pt, RuO_2, IrO_2, etc.) [127]. However, due to the scarcity of resources, it is challenging to realize large-scale industrial applications. Tremendous work has been paid to developing non-noble metal-based electrocatalysts. MOFs have been thought of as promising catalysts for electrocatalytic water splitting due to the inherent ultra-high specific surface area, tunable nanostructure, and porosity. Although MOFs show the advantages mentioned earlier, their wide application has not been realized due to the poor electronic conductivity and unclear reaction mechanism/pathway. In recent

Table 1
Summaries of 1D MOFs and derived materials for electrocatalysis.

Catalyst	Ligand	Structure	Treatment	Target reactions	Performance	Electrolyte	Reference
$Fe/Ni_{2.4}/Co_{0.4}$-MIL-53	1,4-bezenedicarboxylate	Nanorod	_	OER	η_{20} = 236 mV, Tafel slope = 52.2 mV/dec	1.0 M KOH	[55]
Fe_1Ni_4–HHTP MOF	2,3,6,7,10,11-hexahydroxytriphenylene	Nanowire	_	OER	η_{10} = 213 mV	1.0 M KOH	[129]
Co_3O_4/C NAs	2,5-dihydroxytelephthalic acid	Nanowire array	Pyrolysis (Ar)	OER	η_{30} = 318 mV, Tafel slope = 81 mV/dec	1.0 M KOH	[130]
Co_3O_4/C NAs	2,6-naphthalenedicarboxylate	Nanowire array	Pyrolysis (N_2)	OER	η_{10} = 209 mV, Tafel slope = 70 mV/dec	0.1 M KOH	[73]
$Ni@NC_6$-600	2,3-butanedione dioxime	Nanotube	Pyrolysis (Ar)	HER	η_{10} = 181 mV	1.0 M KOH	[132]
S-CoWP@S,N-C	4,4′-trimethylenedipyridine	Nanowire	Pyrolysis (Ar) and phosphorization	HER	η_{10} = 35 mV Tafel slope = 35 mV/dec	0.5 M H_2SO_4	[133]
Co_4Ni_1P	2,5-dihydroxyterephthalic acid	Nanotube	Oxidation and phosphorization	HER	η_{10} = 129 mV, Tafel slope = 53 mV/dec	1.0 M KOH	[134]
Fe_3C@FeN@CNF	2-methylimidazole	Nanofiber	Pyrolysis (N_2)	OER	η_{10} = 450 mV	0.1 M KOH	[114]
ES-CNCo-5	2-methylimidazole, benzimidazole	Nanofiber	Pyrolysis (Ar)	ORR	E_{onset} = 0.91 V, $E_{1/2}$ = 0.836 V	0.1 M KOH	[115]
Co@C@NC	2-methylimidazole	Nanowire	Pyrolysis (Ar/H_2)	ORR	E_{onset} = 0.92 V, $E_{1/2}$ = 0.83 V	0.1 M KOH	[59]
N-GCF-Ni_9Fe_1-800	tetrakis (4-carboxyphenyl)-porphyrin-M (TCPP-M, M = Ni, Fe)	Nanosheet	Pyrolysis (N_2)	ORR	$E_{1/2}$ = 0.83 V	0.1 M KOH	[135]
$Al_2(OH)_2$TCPP-Co	4,4′,4″,4‴-(porphyrin-5,10,15,20-tetrayl)tetrabenzoate	Nano-dendrite	_	CO_2RR	FE_{CO} = 76 %, TON = 1400	0.5 M K_2CO_3	[137]
CdS@Co(BDC) − 20	1,4-benzendicarboxylic acid	Nanorod	_	CO_2RR	FE_{CO} = 92.5 %, TON = 7.3	0.2 M Na_2SO_4	[58]
PCN-223-AA	(5, 10, 15, 20)-tetrakis (4-carboxyphenyl) porphyrin-Co	Nanorod	_	CO_2RR	FE_{CO} = 90.7 %	0.5 M $KHCO_3$	[56]
Cu-SIM NU-1000	1,3,6,8-tetrakis(*p*-benzoic acid)pyrene	Microrod	_	CO_2RR	FE_{CO} = 31 %	0.1 M $NaClO_4$	[57]
Bi SAs/NC	1,3,5-benzenetricarboxylic acid	Nanobundle	Pyrolysis (Ar)	CO_2RR	FE_{CO} = 97 %	0.1 M $NaHCO_3$	[60]

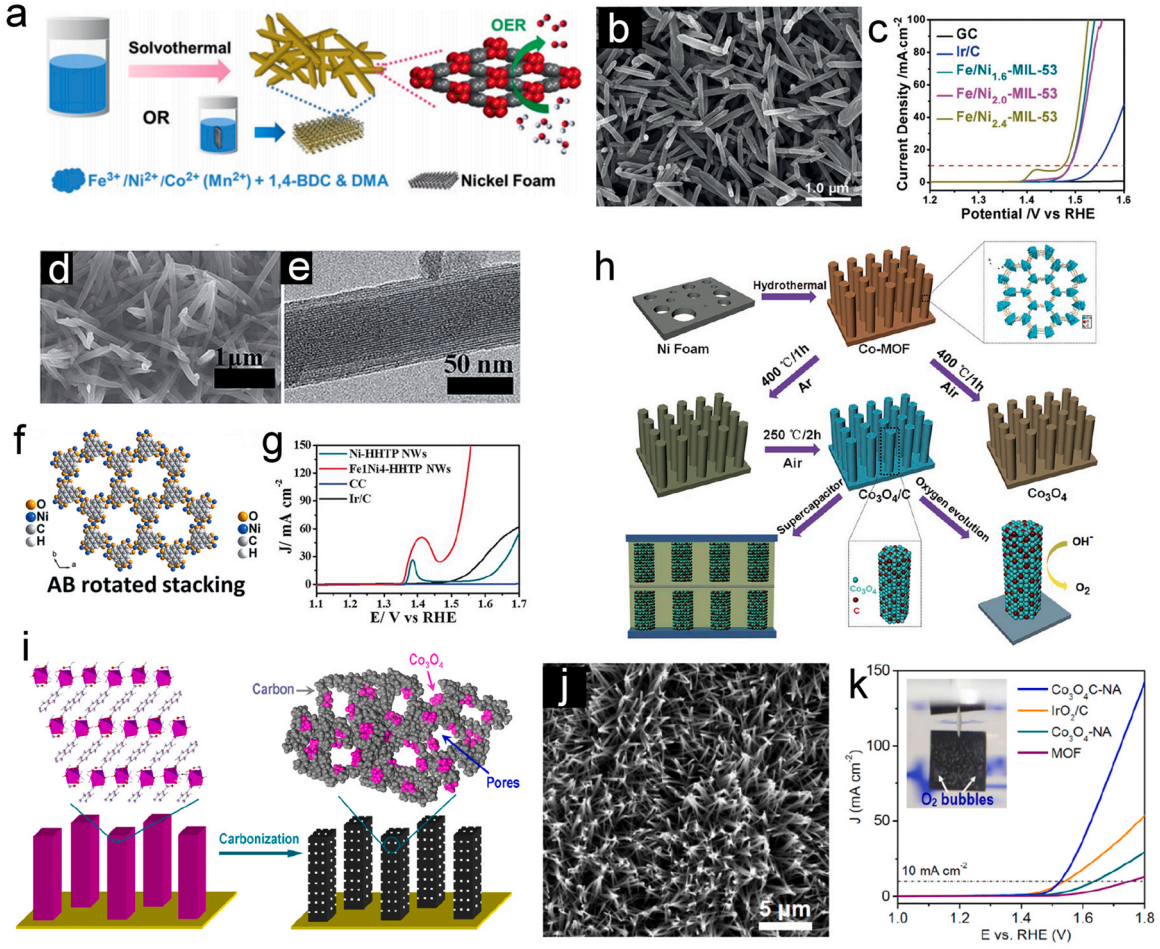

Fig. 9. (a) Schematic illustration of the preparation of Fe/Ni/Co(Mn)-MIL-53 and Fe/Ni/Co(Mn)-MIL-53/NF, and their direct utilization for oxygen evolution reaction. (b) SEM and images of $Fe/Ni_{2.4}$-MIL-53. (c) Linear sweep voltammetry curves toward OER of Fe/Ni_x-MIL-53 (x = 1.6, 2.0, 2.4), commercial Ir/C and pure glassy carbon (GC). (d) SEM images of the Fe_1Ni_4-HHTP nanowire arrays grown on carbon cloth. (e) High-resolution transmission electron microscopy (HRTEM) images of the Fe_1Ni_4-HHTP nanowires. (f) Space-filling drawings of the packing structure of Ni–HHTP along the c direction (blue represents Ni, orange represents oxygen, gray represents carbon, and light gray represents hydrogen). (g) LSV curves of the Ni–HHTP NWs, Fe_1Ni_4-HHTP NWs, carbon cloth (CC), and Ir/C in 1 M KOH. (h) Schematic illustration of the synthesis of hybrid Co_3O_4/C NA electrodes for application in supercapacitors and the oxygen evolution reaction. (i) Fabrication of hybrid Co_3O_4-carbon porous nanowire arrays (j) SEM image of Co_3O_4C-NA. (k) Polarization curves of Co_3O_4C-NA, IrO_2/C, Co_3O_4-NA, and the MOF in an O_2-saturated 0.1 M KOH solution (scan rate 0.5 mV/s). Inset: the optical image of Co_3O_4C-NA directly used as the OER electrode operating at 1.70 V.
(a-c) Reproduced from [55]. (d-g) Reproduced from [129]. (h) Reproduced from [130]. (i-k) Reproduced from [73].

years, MOFs have been widely used as the precursor to achieving metal-carbon composition by calcining MOFs in an inert atmosphere [128]. Continuous conductive carbon substrates can be created through calcination methods to increase electronic conductivity. In addition to the MOF-derived materials, the MOFs can also be used as electrocatalysts and achieve the high activity.

Due to the intrinsic properties of transition metal elements, nickel/cobalt/iron-based compounds and MOFs have been developed for water-splitting [125]. Lang et al. prepared a series of Fe/Ni-based three-metal 1D MOF materials through solvothermal synthesis, which was directly used as high-efficiency electrocatalysts [55]. In a typical synthesis process, 1,4-bezenedicarboxylate (1,4-BDC) was dissolved in N,N-dimethylacetamide (DMA) as a ligand (Fig. 9a). Through solvothermal reaction, rod-shaped bimetallic/trimetallic MOFs with a specific metal element ratio can be achieved (Fig. 9b). It was demonstrated that trimetallic MOFs showed much enhanced OER performance compared with bimetallic MOFs. The optimized $Fe/Ni_{2.4}/Co_{0.4}$-MIL-53 showed a low overpotential of 236 mV (@20 mA/cm^2) and a Tafel slope of 52.2 mV dec^{-1} (Fig. 9c). Besides, this work also found that MOFs can directly grow on nickel foam, and the OER performance can also be further improved due to the direct injection of electrons. More importantly, the MOFs on nickel foam showed good stability during 60 h electrolysis, and the MOF structure was kept after a long-term test. Li et al. also reported the growth of NiFe-MOF (ligand: 2,3,6,7,10,11-hexahydroxytriphenylene) nanowires on conducting carbon cloth (Fig. 9d-f) [129]. The Ni/Fe ratio was adjusted by the concentration of reactants. They found that the Fe_1Ni_4-MOF showed the best OER activity with a low overpotential (@10 mV/cm^2) of 213 mV (Fig. 9g). The incorporation of Fe atoms in Ni-MOF, as well as the unique nanostructures and good conductivity, are demonstrated to contribute to the achieved high OER activity.

In addition to the direct application of MOFs, MOF-derived materials have been widely developed [131]. Zhang et al. first synthesized Co-MOF (ligand: 2,5-dihydroxytelephthalic acid) nanowire on Ni foam and treated the MOF nanowire at 400 ℃ to achieve the Co_3O_4/C array (Fig. 9h) [130]. Benefiting from the large specific area and embedded metal catalysts, the as-prepared Co_3O_4/C array exhibited a moderate OER overpotential (318 mV) at 30 mA/cm^2 and a low Tafel slope (81 mV/dec). Another work reported by Ma et al. synthesized Co-naphthalenedicarboxylate MOF nanowire arrays on Cu foil [73]. The obtained Co_3O_4/C nanowire arrays after carbonization showed a low OER overpotential (~ 290 mV @ 10 mA/cm^2) and strong durability (Fig. 9i-k).

Similarly, the pyrolysis strategy can be applied to achieve a catalyst for HER. In addition to simple pyrolysis, the controllable thermal

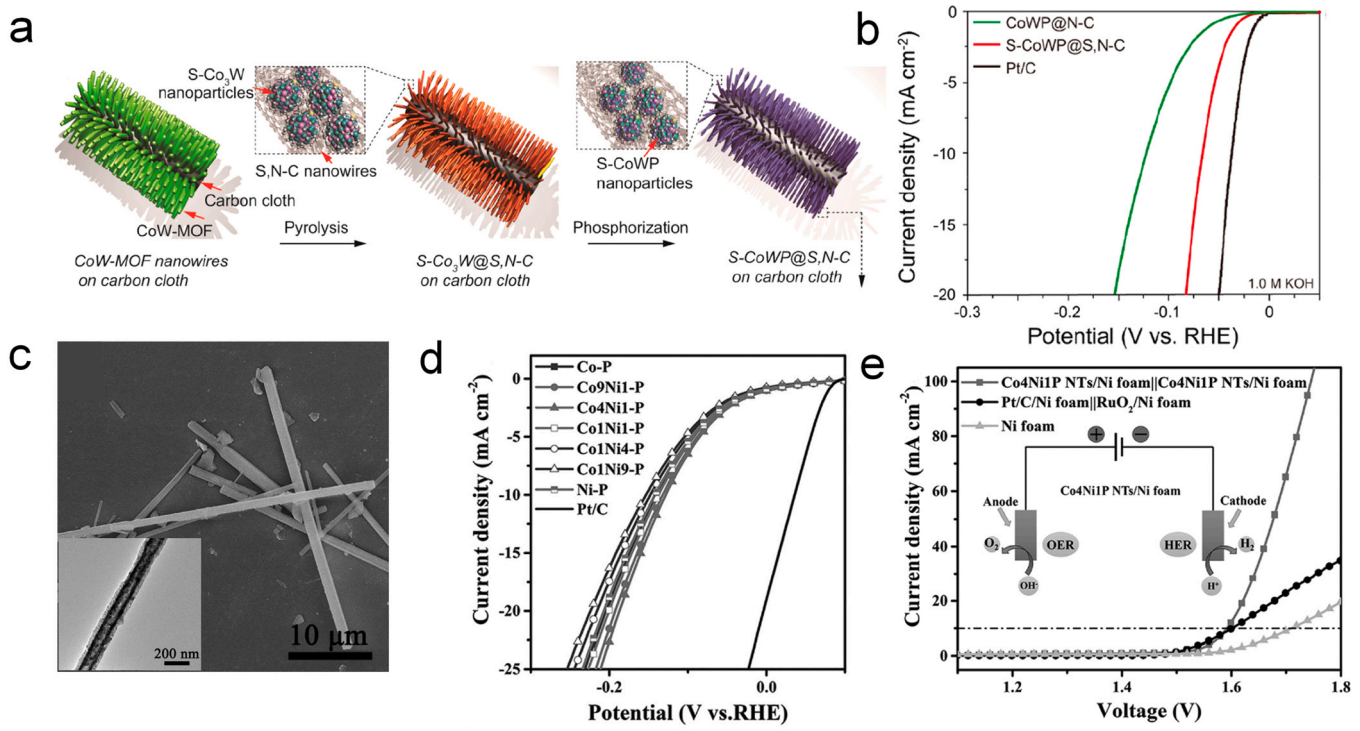

Fig. 10. (a) Schematic of the synthesizing route of S-CoWP@S,N-C. (b) Polarization curves of Ni@NC_4-600, Ni@NC_5-600, Ni@NC_7-600, and Ni@NC_{10}-600. Electrochemical characterization of S-CoW@ (S,N)-C nanowires obtained at various temperatures, S-CoWP@ (S,N)-C nanowire, (S,N)-C nanowires, CoWP@N-C nanowire, and Pt/C electrocatalysts in 0.5 M H_2SO_4 solution. (c) SEM images of MOF-74-Co_4Ni_1. Inset: TEM images of Co_4Ni_1P NTs. (d) HER polarization curves of single-metallic and bimetallic phosphides. (e) The overall water-splitting performance of the Co_4Ni_1P NTs and Pt/C-RuO_2 couple. Inset: the schematic diagram for the overall water splitting reaction in a two-electrode configuration.
(a,b) Reproduced from [133]. (c-e) Reproduced from [134].

treatment of MOFs can result in highly oriented carbon tubes. Cheng et al. reported an in-situ heterogeneous synthesis approach to construct the hierarchical Ni/carbon composition by grafting Ni-doped nitrogen-doped carbon nanotubes onto a MOF-derived carbon substrate [132]. Following the "nanotube tip-growth model" in the synthesis process, the microstructure and size of the prepared hierarchical nickel-based carbon hybrid nanotubes and encapsulated particles are controlled by adjusting the conditions in the thermal process. This method enables the active metal sites to be fully exposed and inhibit the reunition. Weng et al. also reported a similar processing of CoW MOF ($[W(CN)_8](SCN)_3Co_3(C_{13}H_{14}N_2)_6$) nanowires by pyrolysis and phosphorization (Fig. 10a) [133]. The obtained CoWP core showed excellent HER performance with an overpotential of 35 mV in acidic electrolyte and a Tafel slope of 35 mV/dec (Fig. 10b). In addition to carbonization, MOF phosphorization is an effective method to achieve high-performance HER catalyst. Yan et al. synthesized the Co/Ni bimetallic MOF-74 nanowires with different Co/Ni ratios [134]. These samples were firstly oxidized at 350 °C in air and then phosphatized by NaH_2PO_2 at 300 °C in the N_2 atmosphere. The obtained Co_xNi_yP kept the structure of the nanowire, and only the Co_4Ni_1P turned into a nanotube structure (Fig. 10c). When applied in alkaline HER, the optimized overpotential reaches 129 mV, and Tafel slope is 53 mV/dec. Besides, this catalyst also showed a 245 mV overpotential for alkaline OER (Fig. 10d). This provided promising candidates for overall water splitting, which only needed a 1.59 V voltage to reach 10 mA/cm^2 (Fig. 10e).

4.2. Oxygen reduction reaction

Proton exchange membrane fuel cell (PEMFC) is currently a promising technology that converts hydrogen energy efficiently to realize sustainable energy conversion and supply. The performance of the fuel cell device depends largely on the slow-kinetics oxygen reduction reaction (ORR) on the cathode side. Pt-based catalysts can efficiently catalyze ORR, but their high cost, inferior stability, and poor tolerance to methanol under operating conditions hinder their widespread application. Previous studies have shown that high surface area with layered pores, uniform doping, high active site density, and high electrical conductivity are the keys to achieving excellent ORR performance. 1D MOF-derived materials have a well-defined MOF framework and high porosity, which can be transformed into porous carbon with uniform heteroatom decoration through surface pyrolysis under an inert atmosphere. This point makes MOF-derived catalysts potentially rich in activity sites, therefore, MOF-derived carbon composite materials (with metal or metal oxide) have attracted widespread attention as ORR electrocatalysts.

Zeolitic imidazolate frameworks (ZIF) derived material is one of the most attractive catalysts for ORR. The hybrid micro/nanomaterials can enhance performance through a synergistic effect between the compositions. Liu et al. reported the synthesis of Fe_3C nanoparticles embedded in Fe-N-doped porous carbon nanofibers (Fe_3C@FeN@CNF) derived from the 1D ZIF-8@$FeCl_3$@PAN electrospun fibers (Fig. 11a) [114]. They first obtained 1D MOF by electrospinning, a simple method to achieve a 1D nanostructure. In the obtained Fe_3C@FeN@CNF after calcination, abundant active sites are formed, including Fe-N_x, N-C, and Fe_3C/FeNPs encapsulated with carbon, which was uniformly distributed during the thermal treatment. In addition, meso and macroscopic pores are formed simultaneously, contributing to the high specific surface area and more active sites (Fig. 11b). Due to its unique structure and chemical characteristics, the pre-prepared Fe_3C@FeN@CNF showed improved ORR performance, including high activity, durability, and methanol cross-tolerance. In another case, Zhang et al. prepared MOF-derived porous carbon fibers by carbonizing bimetallic ZIF nanofibers assembled by electrospinning (Fig. 11c) [115]. They systematically studied the influence of the zinc-cobalt ratio on the ORR

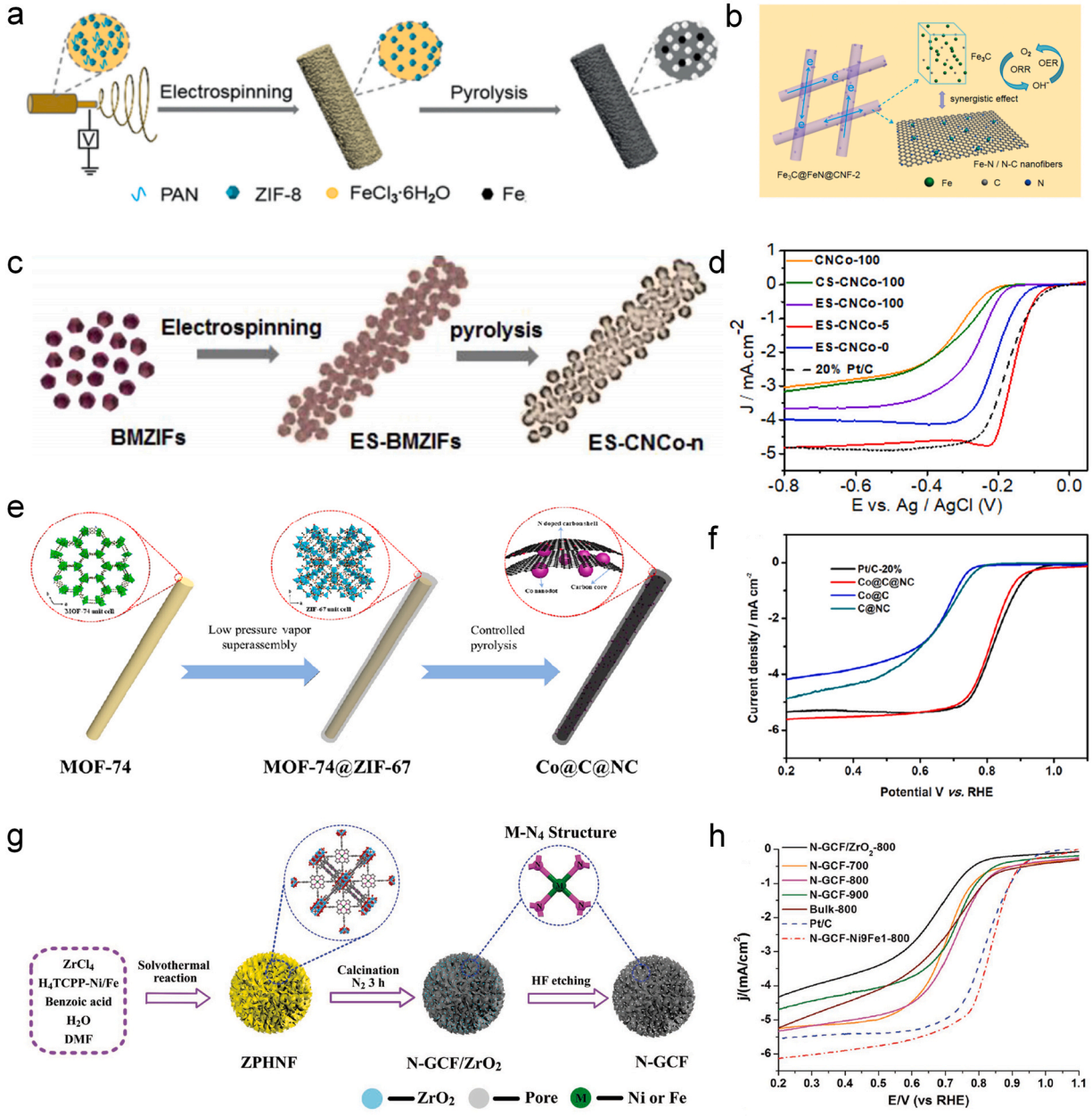

Fig. 11. (a) Schematic illustration for the synthesis of the Fe_3C@FeN@CNF-2 catalyst. (b) Schematic illustration of the synergistic effect among the active sites in Fe_3C@FeN@CNF-2 for bifunctional oxygen catalyst. (c) Schematic illustration of the synthesis process of ES-CNCo-n. (d) LSV curves of CNCo-100, CS-CNCo-100, ES-CNCo-100, ES-CNCo-5, ES-CNCo-0 and Pt/C in O_2-saturated 0.1 M KOH electrolyte. (e) Schematic illustration of the synthesis process and structure of Co@C@NC. (f) Rotating disk electrode (RDE) polarization curves of the synthesized Co@C@NC, Co@C, and Pt/C-20% at a scan rate of 5 mV/s and a rotation speed of 1600 rpm. (g) Schematic of the formation of N-GCF bearing M-N_4 units. (h) LSV curves of Pt/C, N-GCF-800, N-GCF-Ni_9Fe_1-800, and other comparative catalysts at a scan rate of 5 mV/s with 1600 rpm.
(a,b) Reproduced from [114]. (c,d) Reproduced from [115]. (e,f) Reproduced from [59]. (g,h) Reproduced from [135].

performance. The doped porous carbon nanofibers, without any etching or other activation processes, showed excellent electrocatalytic performance compared with the non-electrospinning samples. The samples with a Zn:Co molar ratio of 5:1 show comparable ORR performance comparable to commercial platinum (Fig. 11d). The high catalytic energy is derived from the high density of active sites in the electrospinning MOF fibers, which contribute to the high surface area and uniform N and Co doping in the derivative compositions. Considering the mass transfer in the electrode-electrolyte interface, the 1D porous structure significantly enhanced the oxygen transportation and promoted the reaction kinetics. The above merits of 1D MOF-derived catalysts provide a rational rule to design and achieve high-performance ORR catalysts.

Liu et al. have developed a "MOFs plus ZIFs" strategy to achieve Co nanodots confined in N-doped carbon nanowires [59]. In this work, the MOF-74 nanowire was first synthesized as the core and then treated in 2-methylimidazole (2-MIM) vapor under low pressure to form ZIF-67 on the surface (Fig. 11e). The reaction mechanism is described as: 2-$MIM_{(g)}$ + MOF-$74_{(s)}$ → MOF-74 @ZIF-$67_{(s)}$ + $DHTA_{(g)}$, where DHTA represents 2,5-dihydroxyparaxic acid. This strategy maintained the nanowire structure during pyrolysis and formed a stable carbon shell to confine the Co nanodots. The obtained Co-based catalyst exhibits excellent ORR activity comparable to commercial Pt/C (half-wave potential is 0.83 V vs. RHE) (Fig. 11f).

Similarly, some Zr-based MOFs also have been applied to achieve metal-carbon catalysts for ORR. He et al. synthesized a novel

zirconiumporphyrin MOF hierarchical nano framework structure with effectively and selectively to CO [137]. The typical cobalt-porphyrin

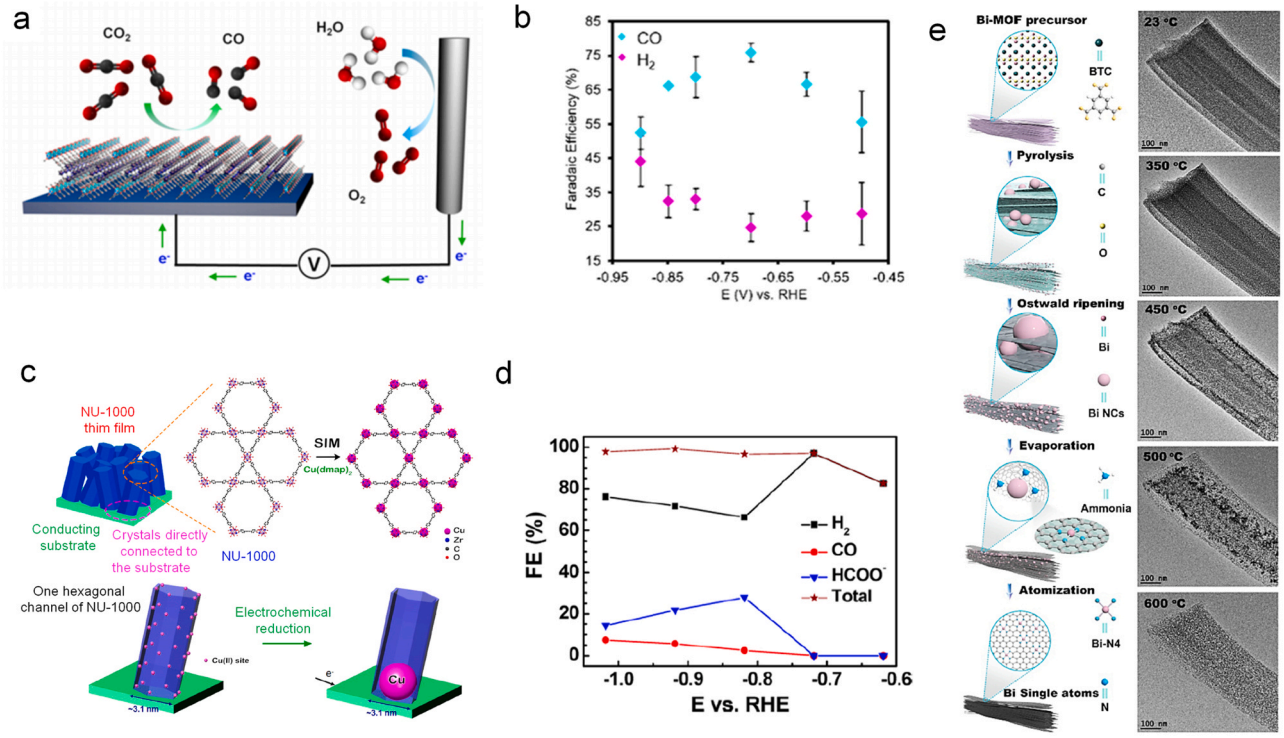

Fig. 12. (a) The MOF is integrated with a conductive substrate to achieve a functional CO_2 electrochemical reduction system. (b) The selectivity for each product is tested over a potential range of −0.5 to −0.9 V vs RHE and reaches upward of 76 % for CO. (c) Schematic representation of SIM to install single-site Cu(II) into the NU-1000 thin film and the electrochemical reduction of Cu(II) to generate metallic Cu nanoparticles. (d) Faradaic efficiencies of generated products based on 30 min of electrolysis of Cu-SIM NU-1000. (e) Scheme of the transformation from Bi-MOF to single Bi atoms and corresponding representative TEM images of Bi-MOF pyrolyzed at different temperatures with the assistance of DCD in situ.
(a,b) Reproduced from [137]. (c,d) Reproduced from [57]. (e) Reproduced from [60].

ordered MOF nanosheet units (Fig. 11g) [135]. The following pyrolysis and acid etching treatment finally generated the graphitic carbon nano framework with M-N_4 units, which is thought as the active core for ORR. When applied in alkaline ORR, the N-GCF catalyst shows optimized activity and stability. The half-wave potential reached 0.83 V vs. RHE and the diffusion-limited current density was 6.19 mA/cm^2 (Fig. 11h). The high activity of this catalyst relies not only on the rich M-N_4 active sites but also on the internal pores, the unique hierarchical structure synergistically promotes the performance of ORR. Based on these merits (active metal sites, porous/hollow structure and conducting carbon substrate), MOF-derived materials have been considered excellent candidates for ORR.

4.3. Carbon dioxide reduction reaction

The carbon dioxide (CO_2) concentration in the atmosphere has exceeded 400 ppm in recent years [136], which indicates that reducing CO_2 emission and increasing carbon neutrality is urgent and impending. One of the most attractive ways to reduce CO_2 emission is to convert inert CO_2 into carbon compounds with high-added value by electrocatalysis. Electrochemical CO_2 reduction reaction (CO_2RR) was thought of as a formidable task due to the high energy barrier to activate stable CO_2 molecules with two double bonds (C═O). The prime issue in reducing carbon dioxide is to realize the chemical adsorption of CO_2 molecules. Researchers have developed diverse catalysts for CO_2RR, such as metal/alloy, metal oxides and sulfides, and MOFs. The metal sites in MOFs have a specific coordination number, which is assumed to activate CO_2 molecules, stabilize selective intermediates, and increase product selectivity. The characteristics of high product selectivity and stability make 1D MOFs promising catalysts in the field of CO_2RR. Kornienko and co-workers reported a nano MOF film that reduced CO_2 MOF showed high selectivity for CO production exceeding 76 %, stability over 7 h, and a turnover number (TON) of 1400. In-situ spectroelectrochemical results proved that the cobalt is the active site and Co^{2+} is reduced to Co^{+} during the catalytic process. Most importantly, most of the catalytic centers in MOF can be oxidized and reduced, which means fully using the catalysts. Mu et al. have reported a work on 1D Co MOF (Co(BDC)) coated on CdS nanowire [58]. Accompanying with the co-catalyst $[Co(bpy)_3]^{2+}$, the CO selectivity of the composite photocatalyst reaches 92.5 %. The MOF layer is demonstrated to facilitate both the charge and mass kinetics in the triphasic (solid-liquid-gas) interface.

Besides Co-based MOF, Zirconium-based MOF also shows activity in CO_2RR. Zhang et al. synthesized porphyrinic Zr-MOF (PCN-223-M) nanorods by adjusting the ratio of zirconium, cobalt porphyrin, and modifiers (Fig. 12a) [56]. The Zr MOF with uncoordinated Zr sites exhibited the highest Faradaic efficiency of 90.7 % when reducing CO_2 to CO (Fig. 12b). Kung et al. used Zr-based MOF (NU-1000) micro rods as the substrate to load Cu(II) clusters as catalysts for CO_2RR [57]. They developed an AIM (atomic layer deposition in MOFs) method to install Cu clusters into the Zr MOF by exposing MOF to vapor-phase $Cu(map)_2$ (dmap = dimethylamino-2-propoxide). The permeated Cu^{2+} coupled with aquo and/or hydroxo ligands generate the tetra-copper(II)oxy in NU-1000. They found that when the electrode potential is below −0.57 V vs. RHE, the Cu^{2+} will be reduced to Cu^0 and generate Cu nanoparticles on the surface of NU-1000 (Fig. 12c). The obtained catalyst showed a high Faradaic efficiency (31%) for CO_2 reduction at −0.82 V vs. RHE and the main product is formate (Fig. 12d).

In addition to the direct application of MOF as the catalyst, the 1D MOF-derived materials also show considerable performance in CO_2RR. Zhang et al. reported the Bi-MOF derived Bi single-atom catalyst for efficient CO_2RR [60]. MOF and dicyandiamide (DCD) were utilized as

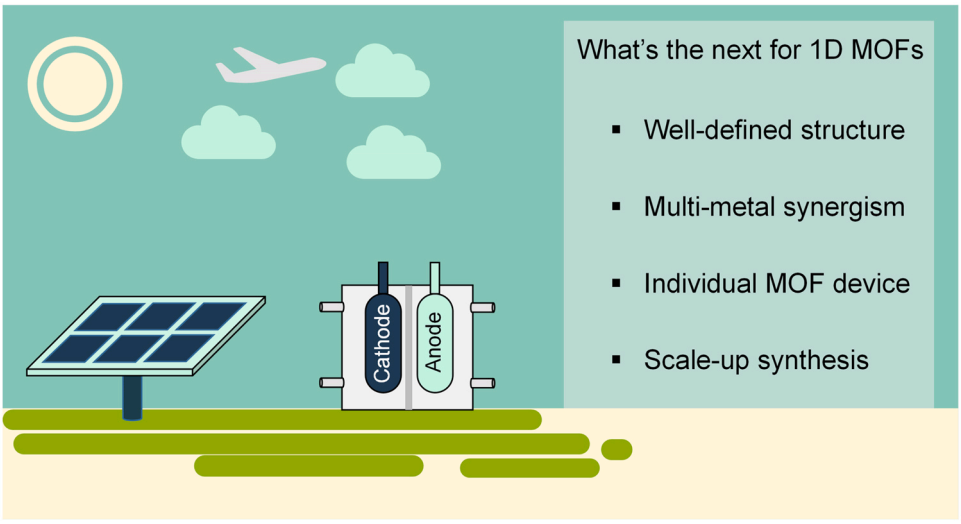

Fig. 13. The schematic illustration of what's next for 1D MOFs for electrocatalysis.

the precursor, which went through the Ostwald ripening, evaporation and atomization process during a temperature-rise period, and the final product is Bi single-atoms on N-doped carbon networks (Fig. 12e). This process was recorded by TEM, which gives a clear demonstration of the pyrolysis pathway. This catalyst also achieved high Faradaic efficiency of 97 % for CO_2 to CO conversion. Although the MOF-derived single-atom catalyst has been widely reported, directly achieving a specific single atom without ZIF-8 is rarely realized. This work provided a reliable investigation of controllably fabricated pure single-atom sites from MOFs.

5. Conclusion and perspective

With the urgent demand for high-performance electrocatalysts to replace noble metals and their compounds in recent years, 1D MOF and its derived materials have become great potential candidates. 1D MOF material combines the characteristics of the 1D structure and MOF material. It not only has adjustable metal centers, abundant active sites, and good flexibility but also has a large surface area, controllable crystal structure, and nano/microporous structure. This review summarizes the synthesis and structure of 1D MOF materials, and briefly describes the application of 1D MOF materials in the field of electrocatalysis. Two methods of preparing 1D MOF materials, i.e., template-assisted and template-free methods, are introduced. Although many 1D MOFs have been achieved, these methods still have some shortcomings such as removing the template and improving crystalline. Therefore, exploring a simple, high-yield, and stable method to prepare high-crystallized 1D MOF materials is still a great challenge. The prepared 1D MOF structures mainly include nanotubes, nanorods, and nanowires, and we have discussed their structural characteristics, respectively. In addition, we also explored the application of 1D MOF material electrocatalysts in electrocatalytic hydrolysis, oxygen reduction, and carbon dioxide reduction. With the continuous development of new characterization technologies, especially the ability to in-situ observe the reaction characteristics of 1D MOF, understanding the structural merits of 1D MOF continues to deepen. Future research on 1D MOF is suggested to consider the fundamental structure regulation and the new strategies to enhance the electrocatalytic activity. The heterogeneous catalysis requires rational material and electrode structure for considerable charge transfer. This point means both the macroscopic and microscopic structures of 1D MOF-based materials are essential. The controllable structure regulation includes the synthesis of pure MOFs, MOF hybrids, MOF-derived materials, and composited structures. Based on the electrocatalysis-oriented regulation of 1D MOFs, enhanced activity and multifunction can thus be achieved.

Although 1D MOF shows excellent potential in the application of electrocatalysis, the field of 1D MOF is still at the start stage, and the application in wide electrocatalysis fields needs to be further developed. What can be expected next for 1D MOFs? First is the well-defined structure of 1D MOFs (Fig. 13). With the development of coordination chemistry and crystallization theory, crystal orientation control could be realized in synthesizing 1D MOFs, which should open a new direction for the precise measurement of 1D MOFs. Second is the multi-metal synergism. The present research mainly focuses on single metal MOFs showing simple properties. The mixed metal sites could be another point for making a complex system for 1D MOFs, not only for the structure complexity but for tailored functionality. According to Sabatier's Principle, the catalyst should have moderate adsorption energy, enabling an optimal energy profile. Based on this theory, the mixed metal sites are usually an effective strategy to adjust the catalysis performance. Considering a MOF structure, different metal-metal coordination could result in diverse interaction ranges and strengths, which could be tunable and favor different reactions. The third is related to the 1D feature, the individual MOF devices. Based on the individual 1D MOF device platforms, measuring well-defined active areas and electron transportation could be an essential methodology. The last is scale-up synthesis. The rapid, low-cost synthesis method should be applied in a practical energy conversion device. The application in the energy industry should be the future of 1D MOFs. It is believed and desired that highly active MOF and MOF-derived electrocatalysts will show a good prospect for various energy-related applications.

Declaration of Competing Interest

The authors declare that they have no known competing financial interests or personal relationships that could have appeared to influence the work reported in this paper.

Acknowledgments

X. Pan and Q. Zhu contributed equally to this work. This work was supported by the National Key Research and Development Program of China (2020YFA0715000), National Natural Science Foundation of China (52127816), Fundamental Research Funds for the Central Universities (2020-YB-014). X. Pan thanks China Scholarship Council for financial support and University of Oxford for research support.

References

[1] P. De Luna, C. Hahn, D. Higgins, S.A. Jaffer, T.F. Jaramillo, E.H. Sargent, Science 364 (2019).
[2] R.M. Bullock, J.G. Chen, L. Gagliardi, P.J. Chirik, O.K. Farha, C.H. Hendon, C.W. Jones, J.A. Keith, J. Klosin, S.D. Minteer, R.H. Morris, A.T. Radosevich, T.B. Rauchfuss, N.A. Strotman, A. Vojvodic, T.R. Ward, J.Y. Yang, Y. Surendranath, Science 369 (2020) eabc3183.
[3] V.R. Stamenkovic, D. Strmcnik, P.P. Lopes, N.M. Markovic, Nat. Mater. 16 (2016) 57–69.
[4] T. Bu, J. Li, H. Li, C. Tian, J. Su, G. Tong, L.K. Ono, C. Wang, Z. Lin, N. Chai, Science 372 (2021) 1327–1332.
[5] G. Ren, J. Liu, J. Wan, Y. Guo, D. Yu, Appl. Energy 204 (2017) 47–65.
[6] J. Ferrero Bermejo, J.F. Gomez Fernandez, F. Olivencia Polo, A. Crespo Márquez, Appl. Sci. 9 (2019) 1844.
[7] P. Albertus, J.S. Manser, S. Litzelman, Joule 4 (2020) 21–32.
[8] W. Luo, F. Li, W. Zhang, K. Han, J.-J. Gaumet, H.-E. Schaefer, L. Mai, Nano Res. 12 (2019) 1025–1031.
[9] J. Zhang, Q. Zhang, X. Feng, Adv. Mater. 31 (2019) 1808167.
[10] Y. Li, Y. Sun, Y. Qin, W. Zhang, L. Wang, M. Luo, H. Yang, S. Guo, Adv. Energy Mater. 10 (2020) 1903120.
[11] M.L. Perry, T.F. Fuller, J. Electrochem. Soc. 149 (2002) S59.
[12] S. Chen, M. Li, M. Gao, J. Jin, M.A. van Spronsen, M.B. Salmeron, P. Yang, Nano Lett. 20 (2020) 1974–1979.
[13] Z.W. Seh, J. Kibsgaard, C.F. Dickens, I. Chorkendorff, J.K. Norskov, T.F. Jaramillo, Science 355 (2017) eaad4998.
[14] B.M. Hunter, H.B. Gray, A.M. Muller, Chem. Rev. 116 (2016) 14120–14136.
[15] C. Wei, R.R. Rao, J. Peng, B. Huang, I.E.L. Stephens, M. Risch, Z.J. Xu, Y. Shao-Horn, Adv. Mater. (2019) e1806296.
[16] X. Zhou, X. Liao, X. Pan, M. Yan, L. He, P. Wu, Y. Zhao, W. Luo, L. Mai, Nano Energy 83 (2021) 105748.
[17] C. Feng, M.B. Faheem, J. Fu, Y. Xiao, C. Li, Y. Li, ACS Catal. 10 (2020) 4019–4047.
[18] A. Dhakshinamoorthy, A.M. Asiri, H. Garcia, Adv. Mater. 31 (2019) e1900617.
[19] Q. Ji, L. Bi, J. Zhang, H. Cao, X.S. Zhao, Energ. Environ. Sci. 13 (2020) 1408–1428.
[20] X. Chia, M. Pumera, Nat. Catal. 1 (2018) 909–921.
[21] B. Cai, R. Hübner, K. Sasaki, Y. Zhang, D. Su, C. Ziegler, M.B. Vukmirovic, B. Rellinghaus, R.R. Adzic, A. Eychmüller, Angew. Chem. Int. Ed. 57 (2018) 2963–2966.
[22] A. Morozan, B. Jousselme, S. Palacin, Energ. Environ. Sci. 4 (2011) 1238–1254.
[23] M. Shao, A. Peles, K. Shoemaker, Nano Lett. 11 (2011) 3714–3719.
[24] X.-F. Yang, A. Wang, B. Qiao, J. Li, J. Liu, T. Zhang, Acc. Chem. Res. 46 (2013) 1740–1748.
[25] A. Wang, J. Li, T. Zhang, Nat. Rev. Chem. 2 (2018) 65–81.
[26] Y. Chen, S. Ji, C. Chen, Q. Peng, D. Wang, Y. Li, Joule 2 (2018) 1242–1264.
[27] J. Lee, O.K. Farha, J. Roberts, K.A. Scheidt, S.T. Nguyen, J.T. Hupp, Chem. Soc. Rev. 38 (2009) 1450–1459.
[28] J. Meng, X. Liu, C. Niu, Q. Pang, J. Li, F. Liu, Z. Liu, L. Mai, Chem. Soc. Rev. 49 (2020) 3142–3186.
[29] A. Mahmood, W. Guo, H. Tabassum, R. Zou, Adv. Energy Mater. 6 (2016) 1600423.
[30] H. Li, M. Eddaoudi, M. O'Keeffe, O.M. Yaghi, Nature 402 (1999) 276–279.
[31] O.K. Farha, J.T. Hupp, Acc. Chem. Res. 43 (2010) 1166–1175.
[32] Q.-L. Zhu, Q. Xu, Chem. Soc. Rev. 43 (2014) 5468–5512.
[33] W. Xuan, C. Zhu, Y. Liu, Y. Cui, Chem. Soc. Rev. 41 (2012) 1677–1695.
[34] O.M. Yaghi, G. Li, H. Li, Nature 378 (1995) 703–706.
[35] J.L. Rowsell, E.C. Spencer, J. Eckert, J.A. Howard, O.M. Yaghi, Science 309 (2005) 1350–1354.
[36] S. Ma, H.-C. Zhou, J. Am. Chem. Soc. 128 (2006) 11734–11735.
[37] W.-H. Chen, M. Vázquez-González, A. Zoabi, R. Abu-Reziq, I. Willner, Nat. Catal. 1 (2018) 689–695.
[38] Y. Chen, V. Lykourinou, T. Hoang, L.-J. Ming, S. Ma, Inorg. Chem. 51 (2012) 9156–9158.
[39] Y. Fu, D. Sun, Y. Chen, R. Huang, Z. Ding, X. Fu, Z. Li, Angew. Chem. Int. Ed. 51 (2012) 3364–3367.
[40] X.-P. Wu, L. Gagliardi, D.G. Truhlar, J. Am. Chem. Soc. 140 (2018) 7904–7912.
[41] S. Zhao, Y. Wang, J. Dong, C.-T. He, H. Yin, P. An, K. Zhao, X. Zhang, C. Gao, L. Zhang, Nat. Energy 1 (2016) 1–10.
[42] J. Duan, S. Chen, C. Zhao, Nat. Commun. 8 (2017) 1–7.
[43] C. Guo, Y. Jiao, Y. Zheng, J. Luo, K. Davey, S.-Z. Qiao, Chem 5 (2019) 2429–2441.
[44] J.-H. Dou, M.Q. Arguilla, Y. Luo, J. Li, W. Zhang, L. Sun, J.L. Mancuso, L. Yang, T. Chen, L.R. Parent, Nat. Mater. 20 (2020) 222–228.
[45] Y. Peng, W. Yang, Sci. China Chem. 62 (2019) 1561–1575.
[46] W. Liu, R. Yin, X. Xu, L. Zhang, W. Shi, X. Cao, Adv. Sci. 6 (2019) 1802373.
[47] K. Yu, X. Pan, G. Zhang, X. Liao, X. Zhou, M. Yan, L. Xu, L. Mai, Adv. Energy Mater. 8 (2018) 1802369.
[48] H. Jin, C. Guo, X. Liu, J. Liu, A. Vasileff, Y. Jiao, Y. Zheng, S.-Z. Qiao, Chem. Rev. 118 (2018) 6337–6408.
[49] M. Luo, S. Guo, Nat. Rev. Mater. 2 (2017) 1–13.
[50] G. Cai, W. Zhang, L. Jiao, S.-H. Yu, H.-L. Jiang, Chem 2 (2017) 791–802.
[51] Q. Liu, L. Xie, X. Shi, G. Du, A.M. Asiri, Y. Luo, X. Sun, Inorg. Chem. Front. 5 (2018) 1570–1574.
[52] R.S. Kumar, S.S. Kumar, M.A. Kulandainathan, Microporous Mesoporous Mat. 168 (2013) 57–64.
[53] X. Cai, Z. Xie, D. Li, M. Kassymova, S.-Q. Zang, H.-L. Jiang, Coord. Chem. Rev. 417 (2020) 213366.
[54] W. Yin, G. Zhang, X. Wang, H. Pang, Adv. Colloid Interface Sci. 298 (2021) 102562.
[55] F.L. Li, Q. Shao, X. Huang, J.P. Lang, Angew. Chem. Int. Ed. 130 (2018) 1906–1910.
[56] X.-D. Zhang, L.-R. Huang, J.-X. Wu, Z.-Y. Gu, Chem. Commun. 57 (2021) 5191–5194.
[57] C.-W. Kung, C.O. Audu, A.W. Peters, H. Noh, O.K. Farha, J.T. Hupp, ACS Energy Lett. 2 (2017) 2394–2401.
[58] Q. Mu, Y. Su, Z. Wei, H. Sun, Y. Lian, Y. Dong, P. Qi, Z. Deng, Y. Peng, J. Catal. 397 (2021) 128–136.
[59] J. Liu, H. Zhang, J. Meng, C. Han, F. Liu, X. Liu, P. Wu, Z. Liu, X. Wang, L. Mai, ACS Appl. Mater. Interfaces 12 (2020) 54545–54552.
[60] E. Zhang, T. Wang, K. Yu, J. Liu, W. Chen, A. Li, H. Rong, R. Lin, S. Ji, X. Zheng, J. Am. Chem. Soc. 141 (2019) 16569–16573.
[61] K. Kida, M. Okita, K. Fujita, S. Tanaka, Y. Miyake, CrystEngComm 15 (2013) 1794–1801.
[62] Y. Pan, Y. Liu, G. Zeng, L. Zhao, Z. Lai, Chem. Commun. 47 (2011) 2071–2073.
[63] Y.-R. Lee, M.-S. Jang, H.-Y. Cho, H.-J. Kwon, S. Kim, W.-S. Ahn, Chem. Eng. J. 271 (2015) 276–280.
[64] M.-H. Chen, Q.-Y. Lu, Y.-M. Li, M.-M. Chu, X.-B. Cao, CrystEngComm 23 (2021) 4327–4335.
[65] W.-w Zhan, Q. Kuang, J.-z Zhou, X.-j Kong, Z.-x Xie, L.-s Zheng, J. Am. Chem. Soc. 135 (2013) 1926–1933.
[66] L. Wang, C. Wang, H. Wang, X. Jiao, Y. Ouyang, X. Xia, W. Lei, Q. Hao, Electrochim. Acta 289 (2018) 494–502.
[67] L.S. Xie, G. Skorupskii, M. Dincă, Chem. Rev 120 (2020), pp. 8536–8580.
[68] M. Ding, X. Cai, H.-L. Jiang, Chem. Sci. 10 (2019) 10209–10230.
[69] L. Li, X. Li, L. Ai, J. Jiang, RSC Adv. 5 (2015) 90265–90271.
[70] P. Pachfule, D. Shinde, M. Majumder, Q. Xu, Nat. Chem. 8 (2016) 718–724.
[71] W. Huan, M. Xing, C. Cheng, J. Li, ACS Sustain. Chem. Eng. 7 (2018) 2245–2254.
[72] Q. Zhang, A. Geng, H. Zhang, F. Hu, Z.H. Lu, D. Sun, X. Wei, C. Ma, Chem. -Eur. J. 20 (2014) 4885–4890.
[73] T.Y. Ma, S. Dai, M. Jaroniec, S.Z. Qiao, J. Am. Chem. Soc. 136 (2014) 13925–13931.
[74] P. Losch, W. Huang, E.D. Goodman, C.J. Wrasman, A. Holm, A.R. Riscoe, J.A. Schwalbe, M. Cargnello, Nano Today 24 (2019) 15–47.
[75] K. Zhou, Y. Li, Angew. Chem. Int. Ed. 51 (2012) 602–613.
[76] P. García-García, M. Müller, A. Corma, Chem. Sci. 5 (2014) 2979–3007.
[77] Y.-S. Wei, M. Zhang, R. Zou, Q. Xu, Chem. Rev. 120 (2020) 12089–12174.
[78] M.B. Stevens, L.J. Enman, A.S. Batchellor, M.R. Cosby, A.E. Vise, C.D.M. Trang, S.W. Boettcher, Chem. Mater. 29 (2016) 120–140.
[79] S. Anantharaj, S.R. Ede, K. Karthick, S. Sam Sankar, K. Sangeetha, P.E. Karthik, S. Kundu, Energ. Environ. Sci. 11 (2018) 744–771.
[80] A.H. Motagamwala, J.A. Dumesic, Chem. Rev. 121 (2021) 1049–1076.
[81] Y. Wang, W. Qiu, E. Song, F. Gu, Z. Zheng, X. Zhao, Y. Zhao, J. Liu, W. Zhang, Natl. Sci. Rev. 5 (2018) 327–341.
[82] A.A. Peterson, J.K. Nørskov, J. Phys. Chem. 3 (2012) 251–258.
[83] Y. Sun, H. Liao, J. Wang, B. Chen, S. Sun, S.J.H. Ong, S. Xi, C. Diao, Y. Du, J.-O. Wang, Nat. Catal. 3 (2020) 554–563.
[84] D.A. Kuznetsov, B. Han, Y. Yu, R.R. Rao, J. Hwang, Y. Román-Leshkov, Y. Shao-Horn, Joule 2 (2018) 225–244.
[85] W. Sheng, Z. Zhuang, M. Gao, J. Zheng, J.G. Chen, Y. Yan, Nat. Commun. 6 (2015) 1–6.
[86] H. Mistry, A.S. Varela, S. Kühl, P. Strasser, B.R. Cuenya, Nat. Rev. Mater. 1 (2016) 1–14.
[87] Y. Wang, H. Su, Y. He, L. Li, S. Zhu, H. Shen, P. Xie, X. Fu, G. Zhou, C. Feng, Chem. Rev. 120 (2020) 12217–12314.
[88] A.P. O'Mullane, Nanoscale 6 (2014) 4012–4026.
[89] T.F. Jaramillo, K.P. Jørgensen, J. Bonde, J.H. Nielsen, S. Horch, I. Chorkendorff, Science 317 (2007) 100–102.
[90] L. Jiao, H.-L. Jiang, Chin. J. Catal. 45 (2023) 1–5.
[91] B. Zhang, K. Jiang, H. Wang, S. Hu, Nano Lett. 19 (2019) 530–537.
[92] T. Wu, S. Sun, J. Song, S. Xi, Y. Du, C. Bo, W.A. Sasangka, H. Liao, C.L. Gan, G. Scherer, Nat. Catal. 2 (2019) 763–772.
[93] X. Liu, R. Guo, K. Ni, F. Xia, C. Niu, B. Wen, J. Meng, P. Wu, J. Wu, X. Wu, Adv. Mater. 32 (2020) 2001136.
[94] J. Wang, M. Yan, K. Zhao, X. Liao, P. Wang, X. Pan, W. Yang, L. Mai, Adv. Mater. 29 (2017) 1604464.
[95] Y. Zhong, S. Wang, M. Li, J. Ma, S. Song, A. Kumar, H. Duan, Y. Kuang, X. Sun, Mater. Today Phys. 18 (2021) 100354.
[96] S. Ren, D. Joulié, D. Salvatore, K. Torbensen, M. Wang, M. Robert, C.P. Berlinguette, Science 365 (2019) 367–369.
[97] D.M. Weekes, D.A. Salvatore, A. Reyes, A. Huang, C.P. Berlinguette, Acc. Chem. Res. 51 (2018) 910–918.
[98] G. Cai, P. Yan, L. Zhang, H.-C. Zhou, H.-L. Jiang, Chem. Rev. 121 (2021) 12278–12326.
[99] K.S. Exner, Chem. Cat. Chem. 11 (2019) 3234–3241.
[100] C. Poidevin, A.A. Auer, Carbon 171 (2021) 618–633.
[101] X. Liu, J. Meng, K. Ni, R. Guo, F. Xia, J. Xie, X. Li, B. Wen, P. Wu, M. Li, Cell Rep. Phys. Sci. 1 (2020) 100241.
[102] J. Parrondo, T. Han, E. Niangar, C. Wang, N. Dale, K. Adjemian, V. Ramani, Proc. Natl. Acad. Sci. USA 111 (2014) 45–50.
[103] Z. Liang, C. Qu, D. Xia, R. Zou, Q. Xu, Angew. Chem. Int. Ed. 57 (2018) 9604–9633.
[104] A. Kuc, A. Enyashin, G. Seifert, J. Phys. Chem. B 111 (2007) 8179–8186.
[105] V. Stavila, A.A. Talin, M.D. Allendorf, Chem. Soc. Rev. 43 (2014) 5994–6010.
[106] J. Hu, T.W. Odom, C.M. Lieber, Acc. Chem. Res. 32 (1999) 435–445.

[107] R.C. Arbulu, Y.B. Jiang, E.J. Peterson, Y. Qin, Angew. Chem. Int. Ed. 57 (2018) 5813–5817.
[108] N. Liu, Y. Yao, J.J. Cha, M.T. McDowell, Y. Han, Y. Cui, Nano Res. 5 (2012) 109–116.
[109] B. Wang, M. Zhao, L. Li, Y. Huang, X. Zhang, C. Guo, Z. Zhang, H. Cheng, W. Liu, J. Shang, Natl. Sci. Rev. 7 (2020) 46–52.
[110] C. Wu, L.-Y. Chou, L. Long, X. Si, W.-S. Lo, C.-K. Tsung, T. Li, ACS Appl. Mater. Inter. 11 (2019) 35820–35826.
[111] B. Wang, W. Liu, W. Zhang, J. Liu, Nano Res. 10 (2017) 3826–3835.
[112] L. Zou, C.-C. Hou, Z. Liu, H. Pang, Q. Xu, J. Am. Chem. Soc. 140 (2018) 15393–15401.
[113] T. Bataille, S. Bracco, A. Comotti, F. Costantino, A. Guerri, A. Ienco, F. Marmottini, CrystEngComm 14 (2012) 7170–7173.
[114] J.T. Liu, Y. Xie, Q. Gao, F.H. Cao, L. Qin, Z.Y. Wu, W. Zhang, H. Li, C.L. Zhang, Eur. J. Inorg. Chem. 2020 (2020) 581–589.
[115] C.-L. Zhang, B.-R. Lu, F.-H. Cao, Z.-Y. Wu, W. Zhang, H.-P. Cong, S.-H. Yu, Nano Energy 55 (2019) 226–233.
[116] J.-H. Dou, M.Q. Arguilla, Y. Luo, J. Li, W. Zhang, L. Sun, J.L. Mancuso, L. Yang, T. Chen, L.R. Parent, Nat. Mater. 20 (2021) 222–228.
[117] R.W. Day, D.K. Bediako, M. Rezaee, L.R. Parent, G. Skorupskii, M.Q. Arguilla, C.H. Hendon, I. Stassen, N.C. Gianneschi, P. Kim, ACS Cent. Sci. 5 (2019) 1959–1964.
[118] D.K. Unruh, K. Gojdas, A. Libo, T.Z. Forbes, J. Am. Chem. Soc. 135 (2013) 7398–7401.
[119] J. Dong, J. Zhang, 13-Maya blue pigments derived from clay minerals, in: A. Wang, W. Wang (Eds.), Nanomaterials from Clay Minerals, Elsevier, 2019, pp. 627–661.
[120] X.F. Lu, L. Yu, X.W.D. Lou, Sci. Adv. 5 (2019) eaav6009.
[121] W. Zhang, Z.-Y. Wu, H.-L. Jiang, S.-H. Yu, J. Am. Chem. Soc. 136 (2014) 14385–14388.
[122] Y.P. Zhu, J. Yin, E. Abou-Hamad, X. Liu, W. Chen, T. Yao, O.F. Mohammed, H.N. Alshareef, Adv. Mater. 32 (2020) 1906368.
[123] K. Huang, L.L. Guo, D.F. Wu, Mater. Res Express 6 (2019) 125101.
[124] J. Liu, D. Zhu, C. Guo, A. Vasileff, S.Z. Qiao, Adv. Energy Mater. 7 (2017) 1700518.
[125] L. Han, S. Dong, E. Wang, Adv. Mater. 28 (2016) 9266–9291.
[126] J. Song, C. Wei, Z.F. Huang, C. Liu, L. Zeng, X. Wang, Z.J. Xu, Chem. Soc. Rev. 49 (2020) 2196–2214.
[127] D. Zhao, Z. Zhuang, X. Cao, C. Zhang, Q. Peng, C. Chen, Y. Li, Chem. Soc. Rev. 49 (2020) 2215–2264.
[128] A. Han, B. Wang, A. Kumar, Y. Qin, J. Jin, X. Wang, C. Yang, B. Dong, Y. Jia, J. Liu, Small Methods 3 (2019) 1800471.
[129] W.-H. Li, J. Lv, Q. Li, J. Xie, N. Ogiwara, Y. Huang, H. Jiang, H. Kitagawa, G. Xu, Y. Wang, J. Mater. Chem. A 7 (2019) 10431–10438.
[130] C. Zhang, J. Xiao, X. Lv, L. Qian, S. Yuan, S. Wang, P. Lei, J. Mater. Chem. A 4 (2016) 16516–16523.
[131] C. Wang, Y.V. Kaneti, Y. Bando, J. Lin, C. Liu, J. Li, Y. Yamauchi, Mater. Horiz. 5 (2018) 394–407.
[132] N. Cheng, N. Wang, L. Ren, G. Casillas-Garcia, N. Liu, Y. Liu, X. Xu, W. Hao, S.X. Dou, Y. Du, Carbon 163 (2020) 178–185.
[133] B. Weng, C.R. Grice, W. Meng, L. Guan, F. Xu, Y. Yu, C. Wang, D. Zhao, Y. Yan, ACS Energy Lett. 3 (2018) 1434–1442.
[134] L. Yan, L. Cao, P. Dai, X. Gu, D. Liu, L. Li, Y. Wang, X. Zhao, Adv. Funct. Mater. 27 (2017) 1703455.
[135] T. He, B. Ni, Y. Ou, H. Lin, S. Zhang, C. Li, J. Zhuang, W. Hu, X. Wang, Small Methods 2 (2018) 1800068.
[136] R. Monastersky, Nat. N. 497 (2013) 13.
[137] N. Kornienko, Y. Zhao, C.S. Kley, C. Zhu, D. Kim, S. Lin, C.J. Chang, O.M. Yaghi, P. Yang, J. Am. Chem. Soc. 137 (2015) 14129–14135.